

# Machine learning one-dimensional spinless trapped fermionic systems with neural-network quantum states

J. W. T. Keeble<sup>1,\*</sup>, M. Drissi<sup>1,2,†</sup>, A. Rojo-Francàs<sup>3,4</sup>, B. Juliá-Díaz<sup>3,4</sup> and A. Rios<sup>1,3,4</sup>

<sup>1</sup>*Department of Physics, University of Surrey, Guildford GU2 7XH, United Kingdom*

<sup>2</sup>*TRIUMF, 4004 Wesbrook Mall, Vancouver, BC V6T 2A3, Canada*

<sup>3</sup>*Departament de Física Quàntica i Astrofísica (FQA),  
Universitat de Barcelona (UB), c. Martí i Franquès 1, 08028, Barcelona, Spain*

<sup>4</sup>*Institut de Ciències del Cosmos (ICCUB), Universitat de Barcelona (UB),  
c. Martí i Franquès 1, 08028, Barcelona, Spain*

(Dated: April 11, 2023)

We compute the ground-state properties of fully polarized, trapped, one-dimensional fermionic systems interacting through a gaussian potential. We use an antisymmetric artificial neural network, or neural quantum state, as an ansatz for the wavefunction and use machine learning techniques to variationally minimize the energy of systems from 2 to 6 particles. We provide extensive benchmarks with other many-body methods, including exact diagonalisation and the Hartree-Fock approximation. The neural quantum state provides the best energies across a wide range of interaction strengths. We find very different ground states depending on the sign of the interaction. In the non-perturbative repulsive regime, the system asymptotically reaches crystalline order. In contrast, the strongly attractive regime shows signs of bosonization. The neural quantum state continuously learns these different phases with an almost constant number of parameters and a very modest increase in computational time with the number of particles.

## I. INTRODUCTION

The emergence of Machine Learning (ML) within science has revolutionized numerous fields, from ab-initio quantum chemistry to cosmology, by directly ‘learning’ from data to understand physical phenomena [1]. Learning algorithms based on neural networks are underpinned by Universal Approximation Theorems (UATs), which allow for, in principle, an arbitrary accuracy of data representation. UATs are, however, *existence* theorems, which state that such benefits are possible, but do not necessarily indicate *how* such benefits are achieved [2–5]. This allows for a wide range of research to build ML-based algorithms that represent physical phenomena, most notably the quantum many-body problem.

The first use of ML in a quantum many-body system was pioneered in Ref. [6] and focused on discrete systems. Since then, several different physical systems have been tackled with these techniques [7–11]. Applications in quantum chemistry, like FermiNet [12, 13] or PauliNet [14, 15], have paved the way for accurate solutions of the electronic Schrödinger equation [16–19]. The marriage of quantum states and neural networks has lead to the novel field of neural-network quantum states (NQSSs) [9].

ML-based NQS approaches solve the Schrödinger equation variationally by representing the wavefunction as a neural network [6]. NQSSs are formulated so that they explicitly keep the antisymmetry of the many-body wavefunction. So far, there are indications that NQSSs can compress the relevant information of many-body wavefunction in a compact way [6, 8, 12–14, 20–22]. While

NQSSs come in many different setups, first-quantized, real-space formulations are often employed to perform integrals over many-particle variables, using Monte Carlo (MC) techniques. This approach essentially boils down to variational Monte Carlo (VMC) [23] with more expressible ansätze. Moreover, the use of a ML framework allows for efficient updates of NQS parameters via Automatic Differentiation (AD) techniques [24]. Having direct access to the many-body wavefunction has the added benefit of allowing, in principle, the calculation of any many-body observable and, potentially, the simulation of many-body dynamics [6].

Our focus here is on providing a minimal implementation of a NQS for solutions of the many-body Schrödinger equation in a simple system of potential interest in condensed matter. As a proof-of-concept, we turn our attention to one-dimensional systems, which are computationally simpler than three-dimensional ones, and fully polarized (or spinless) fermions. We assume the fermions to be in a harmonic trap and their pair-wise interactions are characterised via a finite-range interaction. This exploratory work acts as a stepping stone towards the creation of NQS that describe more complex nuclear systems [25–29].

Under certain circumstances, bosons and fermions can hold similar properties. This phenomenon is referred to as the Fermi-Bose duality and is particularly prominent in one spatial dimension settings [30, 31]. The duality manifests itself with strongly-interacting fermions acting like weakly-interacting bosons and vice versa [32]. Traditionally, the duality has been discussed in terms of spin-1/2 particles with contact interactions [33, 34]. In the case of fully polarized fermions, the Pauli exclusion principle restricts our wavefunction ansatz to be antisymmetric with respect to particle position, which results in

\* [j.keeble@surrey.ac.uk](mailto:j.keeble@surrey.ac.uk)

† [mdrissi@triumf.ca](mailto:mdrissi@triumf.ca)

the physical effect of forbidding S-wave interactions and primarily consisting of P-wave interactions [32, 35–38].

Interestingly, the considered quantum many-body problem is nowadays within reach experimentally in ultracold atomic laboratories worldwide [39, 40]. Starting from the production of degenerate Fermi gases [41], experimentalists are able to tune the interactions among fermions and study the equation of state [42] and even produce few-fermion systems in a controlled way [43].

In this paper, we benchmark a minimalist implementation of the FermiNet NQS in Ref. [12] to represent one-dimensional trapped fermionic systems. In Sec. II, we define the system and the Hamiltonian we consider. We provide a detailed explanation of the NQS and the benchmark many-body methods in Sec. III. A detailed analysis of the obtained results is provided in IV. We provide conclusions and an outlook of future research in Sec. V.

## II. SYSTEM AND HAMILTONIAN

We study a system of  $A$  identical fermions with mass  $m$  trapped in a harmonic trap of frequency  $\omega$ . We neglect spin in the following, assuming that the system is fully polarized. We focus on a finite-range gaussian inter-particle interaction, which yields the following Hamiltonian in real space:

$$\hat{H} = -\frac{\hbar^2}{2m} \sum_{i=1}^A \nabla_i^2 + \frac{1}{2} m\omega^2 \sum_{i=1}^A x_i^2 + \frac{V}{\sqrt{2\pi}\sigma} \sum_{i < j} e^{-\frac{(x_i - x_j)^2}{2\sigma^2}}. \quad (1)$$

The gaussian interaction is characterised by an interaction strength,  $V$ , and an interaction range,  $\sigma$ . We choose these so that, in the limit  $\sigma \rightarrow 0$  the potential becomes a contact interaction,  $\rightarrow V\delta(x_i - x_j)$ .

We use harmonic oscillator (HO) units throughout the remainder of this work: lengths are defined in terms of  $a_{\text{ho}} = \sqrt{\frac{\hbar}{m\omega}}$  and energies are measured in units of  $\hbar\omega$ . The Hamiltonian becomes

$$\hat{H} = -\frac{1}{2} \sum_{i=1}^A \nabla_i^2 + \frac{1}{2} \sum_{i=1}^A x_i^2 + \frac{V_0}{\sqrt{2\pi}\sigma_0} \sum_{i < j} e^{-\frac{(x_i - x_j)^2}{2\sigma_0^2}}. \quad (2)$$

The interaction range is redefined, so that  $\sigma_0 = \sigma/a_{\text{ho}}$ . The dimensionless interaction strength  $V_0$  is related to the dimensionfull constant  $V$  by  $V_0 = V/(a_{\text{ho}}\hbar\omega)$ .

For spinless fermions, the presence of a finite range interaction is a necessary condition to observe interaction effects. Indeed, without spin, the many-body wavefunction is antisymmetric on the space variables  $\{x_i, i = 1, \dots, A\}$ . For pairs of particles  $i \neq j$ , the wavefunction cancels whenever  $x_i = x_j$ . As a consequence, contact interactions

do not contribute to the energy of the system. Naively, one expects such interaction effects to be relatively small compared to interactions of the same strength in the spinful case.

The specific choice of a gaussian form factor for the interaction is dictated mostly by practical reasons [33, 39]. First and foremost, because of the simplicity of the associated integrals, gaussians can be easily handled in many-body simulations, including exact diagonalisation [44] as well as stochastic methods [45]. Second, as already noted above, normalised gaussian interactions can be used to approach the contact interaction limit by tuning the range parameter  $\sigma \rightarrow 0$ . Third, our ultimate goal is to simulate nuclear physics systems. Finite-range interactions are particularly relevant for nuclear physics applications, where the range of the interaction is related to the mass of meson force carriers [46]. There are examples of nuclear interactions with a gaussian (or a sum of gaussians) form factor, like the Gogny force [46]. We also note that gaussian interactions have been extensively used in the analysis of several many-body systems, including the so-called "gaussian characterisation" of universal behavior [47].

### A. Non-interacting case

Before providing more details on how interactions are considered, we turn our attention briefly to the analytically solvable, non-interacting case. In the absence of spin, each fermion can occupy a single-particle level with energy  $\epsilon_n = n + 1/2$  characterised by a single quantum number  $n$ . The single-particle wavefunctions are HO eigenstates,

$$\varphi_n(x) = \mathcal{N}_n e^{-\frac{x^2}{2}} H_n(x), \quad (3)$$

with  $H_n(x)$  the  $n^{\text{th}}$  Hermite polynomial and  $\mathcal{N}_n = 1/\sqrt{2^n n! \sqrt{\pi}}$ , a normalization constant. The many-body wavefunction is a pure Slater determinant. It factorises into an overall gaussian envelope, times a determinant involving only Hermite polynomials:

$$\Psi(x_1, \dots, x_A) = \frac{1}{\sqrt{A!}} \left[ \prod_{n=0}^{A-1} \mathcal{N}_n e^{-\frac{x_n^2}{2}} \right] \times \begin{vmatrix} H_0(x_1) & H_0(x_2) & \dots & H_0(x_A) \\ H_1(x_1) & H_1(x_2) & \dots & H_1(x_A) \\ \vdots & \vdots & \ddots & \vdots \\ H_{A-1}(x_1) & H_{A-1}(x_2) & \dots & H_{A-1}(x_A) \end{vmatrix}. \quad (4)$$

This, in turn, may be further simplified in terms of Vandermonde determinants [33, 48].

The total energy of the many-body system is easily obtained by adding up all the occupied single-particle state energies,

$$E_A = \sum_{n=0}^{A-1} \epsilon_n = \frac{A^2}{2}, \quad (5)$$

and it scales with  $A^2$ . These non-interacting benchmarks are useful, especially in setting up the NQS ansatz. In particular, as we explain below, we pre-train neural networks to the non-interacting solution. This provides an initial confined, stable and physical result, from which we can start the relatively demanding variational simulations.

## B. Density matrices

We can further characterise correlations in the system by employing many-body density matrices [49, 50]. The one-body density matrix (OBDM) for the  $A$ -body system is defined as the following  $A - 1$  integral over the many-body wave function,

$$\rho(x'_1, x_1) = A \int dx_2 \dots dx_A \Psi^*(x'_1, x_2, \dots, x_A) \times \Psi(x_1, x_2, \dots, x_A). \quad (6)$$

The diagonalisation of  $\rho$  in the space representation,

$$\int d\bar{x} \rho(x, \bar{x}) \phi_\alpha(\bar{x}) = n_\alpha \phi_\alpha(x), \quad (7)$$

gives rise to the so-called natural orbitals,  $\phi_\alpha(x)$ , as well as the occupation numbers,  $n_\alpha$ .  $\alpha$  is a discrete index running, in principle, from  $\alpha = 0$  to infinity. The spectral decomposition of the OBDM allows for the following expansion:

$$\rho(x'_1, x_1) = \sum_{\alpha=0}^{\infty} n_\alpha \phi_\alpha^*(x'_1) \phi_\alpha(x_1). \quad (8)$$

We work with a normalisation such that  $\sum_\alpha n_\alpha = A$ .

In a non-interacting or a Hartree-Fock (HF) ground-state, one finds

$$n_\alpha = \begin{cases} 1, & \alpha < A, \\ 0, & \alpha \geq A. \end{cases} \quad (9)$$

The sum in Eq. (3) is thus naturally truncated to  $A$  terms. In addition, for the non-interacting case, the natural orbitals correspond to the single-particle states of Eq. (3). Performing the sum for a non-interacting system, one finds that the OBDMs have the form

$$\rho(x'_1, x_1) = \frac{e^{-\frac{x'_1}{2} - \frac{x_1}{2}}}{\sqrt{\pi}} \mathcal{R}^{(A)}(x'_1, x_1), \quad (10)$$

where  $\mathcal{R}^{(A)}(x'_1, x_1)$  is a polynomial of at most order  $A - 1$  in both  $x_1$  and  $x'_1$  [51, 52].

One can also prove that a system with the occupation numbers described by Eq. (9) has a Slater determinant as a many-body wavefunction [53]. In other words, deviations from the uncorrelated values  $n_m = 1$  and  $n_m = 0$  provide a solid metric for intrinsic correlations in the system [38].

The two-body density matrix (TBDM) is also an excellent indicator of intrinsic correlations. It is usually defined as [49],

$$\Gamma(x'_1, x'_2; x_1, x_2) = \binom{A}{2} \int dx_3 \dots dx_A \Psi^*(x'_1, x'_2, \dots, x_A) \times \Psi(x_1, x_2, \dots, x_A).$$

The positive-definite diagonal elements of this matrix provide the pair correlation function of the system,

$$g(x_1, x_2) = \Gamma(x'_1 = x_1, x'_2 = x_2; x_1, x_2), \quad (11)$$

which has a direct physical interpretation in terms of the probability of finding a particle at position  $x_1$  when another one lies at  $x_2$  [50]. Closed expressions can be found for this object in the non-interacting case, too. In this case, the correlation function has a structure of the type

$$g(x_1, x_2) = \frac{e^{-x_1^2 - x_2^2}}{\pi} (x_1 - x_2)^2 \mathcal{G}^{(A)}(x_1, x_2), \quad (12)$$

where  $\mathcal{G}^{(A)}(x_1, x_2)$  is again a polynomial of at most order  $A - 1$  in both  $x_1$  and  $x_2$ .

## III. METHODS

We now describe the different quantum many-body approaches that we have used to benchmark our few-body solutions. We start by providing a description of the NQS ansatz, and then move on to describe briefly the exact diagonalisation method and the Hartree-Fock approximation for the cases with  $A > 1$ . We end the section with a description of two additional numerical methods employed to benchmark specifically the  $A = 2$  case.

### A. Neural quantum states

#### 1. Architecture

Our NQS ansatz is a fully antisymmetric neural network, inspired by the implementation of FermiNet [12]. The input to our network are the  $A$  positions of fermions in the system,  $\{x_i, i = 1, \dots, A\}$ , and the output is the many-body wavefunction  $\Psi_\theta(x_1, \dots, x_A)$ , which depends on a series of network weights and biases, succinctly summarised by a multidimensional variable  $\theta$ . We provide a schematic representation of the network architecture in Fig. 1. The network is composed of 4 core components: equivariant layers, generalised Slater matrices (GSMS), log-envelope functions, and a summed signed-log determinant function. We now proceed to describe each of the 4 core components of our NQS.

In order for the NQS to respect antisymmetry, we enforce permutation equivariance across the network. The

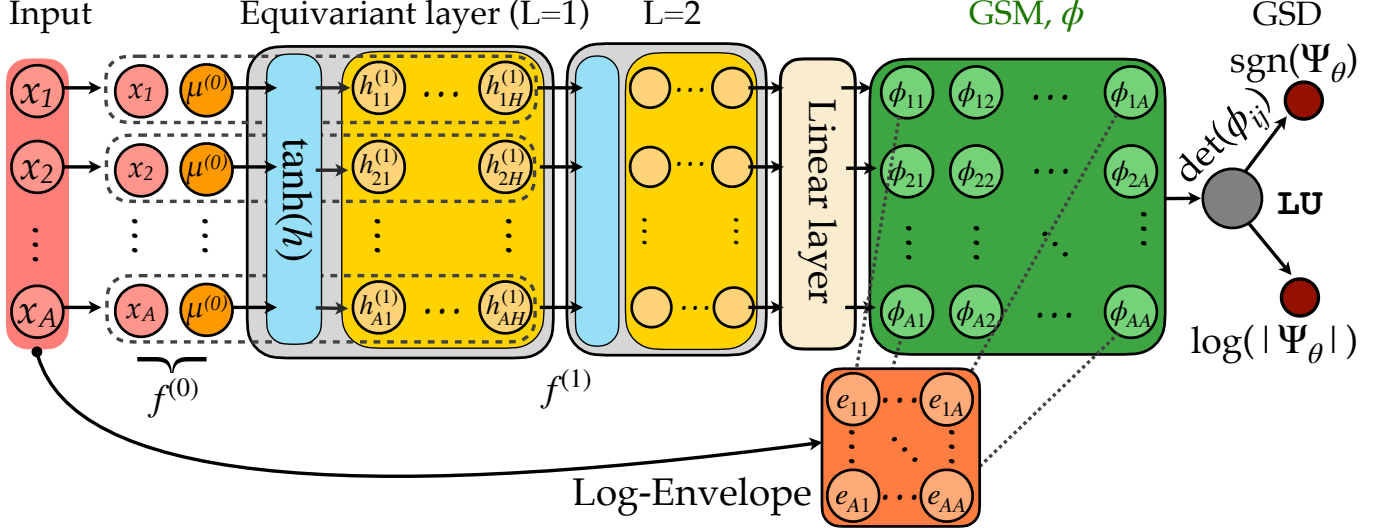


FIG. 1. The NQS ansatz of this work for  $L = 2$  equivariant layers of  $H$  hidden nodes. The input to the network are the  $\{x_i, i = 1, \dots, A\}$  particle positions. These are processed by 2 equivariant layers (light gray areas), to ensure that the NQS maintains equivariance throughout its forward pass. The grey dashed lines denote all nodes involved in the linear equivariant mapping, which is subsequently shared over all input nodes and passed through a hyperbolic tangent function (blue area). The final embeddings are projected via a linear layer into an  $A \times A$  matrix (green area), which is element-wise multiplied with the log-envelope layer (orange area) before taking a determinant. In a final step, a LU decomposition is used to find the sign and logarithm of the absolute value of the many-body wavefunction,  $\Psi$ .

inputs to our network are an  $A$ -dimensional vector,  $x \in \mathbb{R}^A$ . The outputs of an equivariant layer,  $h_i(x)$ , are such that any permutation of the input variables,  $\pi$ , permutes the outputs too,  $h_i(x_{\pi(1)}, \dots, x_{\pi(A)}) = h_{\pi(i)}(x_1, \dots, x_A)$ .

To ensure equivariance, we follow the methodology of Ref. [54]. We preprocess the input layer by adding a permutation-invariant feature, which in our case is the the mean many-body position,  $\mu^{(0)} = \frac{1}{A} \sum_{i=1}^A x_i$ . The input to the first layer is then a concatenation of  $x \in \mathbb{R}^A$ , and the corresponding mean position,  $\mu^{(0)} \in \mathbb{R}$ . This defines an input feature  $f^{(0)} \in \mathbb{R}^{A \times 2}$ , such that

$$f_{ij}^{(0)} = \begin{cases} x_i & \text{if } j = 1 \\ \mu^{(0)} & \text{if } j = 2 \end{cases} \quad (13)$$

The first equivariant layer ( $L = 1$ ) of the network is shown in a grey area in Fig. 1. Each row of the input feature is passed through a shared layer to build an intermediate  $H$ -dimensional representation of the positions,  $h^{(1)} \in \mathbb{R}^{A \times H}$  (yellow area in Fig. 1). This layer consists of a linear transformation with weights  $W^{(1)} \in \mathbb{R}^{2 \times H}$  and biases  $b^{(1)} \in \mathbb{R}^{1 \times H}$  combined with a non-linear activation function. We choose a hyperbolic tangent activation function, since this is continuous and differentiable, a requirement when it comes to computing many-body kinetic energies. Explicitly, each row  $h_i^{(1)} \in \mathbb{R}^{1 \times H}$  reads

$$h_i^{(1)} = \tanh \left( f_i^{(0)} W^{(1)} + b^{(1)} \right). \quad (14)$$

The second equivariant layer ( $L = 2$ ) takes the output of the first layer,  $h^{(1)}$ , and their column-wise averages

$\mu^{(1)} \in \mathbb{R}^H$ , to define a new input feature  $f^{(1)} \in \mathbb{R}^{A \times 2H}$  such that

$$f_{ij}^{(1)} = \begin{cases} h_{ij}^{(1)} & \text{if } j \leq H \\ \mu_i^{(1)} & \text{if } j > H \end{cases} \quad (15)$$

Similarly to the first layer, the input feature is passed through a shared layer with weights  $W^{(2)} \in \mathbb{R}^{2H \times H}$ , biases  $b^{(2)} \in \mathbb{R}^{1 \times H}$  and the same non-linear activation function. A residual connection is also added so that each row of the output  $h_i^{(2)} \in \mathbb{R}^{1 \times H}$  explicitly reads

$$h_i^{(2)} = \tanh \left( f_i^{(1)} W^{(2)} + b^{(2)} \right) + h_i^{(1)}. \quad (16)$$

After the second equivariant layer,  $h^{(2)}$  goes through a linear layer (see beige area in Fig. 1) with shared weights  $W^{(M)} \in \mathbb{R}^{H \times A}$  and biases  $b^{(M)} \in \mathbb{R}^{1 \times A}$  to output a matrix  $M \in \mathbb{R}^{A \times A}$ . Each row  $M_i \in \mathbb{R}^{1 \times A}$  reads

$$M_i = h_i^{(2)} W^{(M)} + b^{(M)}. \quad (17)$$

At this stage, asymptotic boundary conditions, such as the wave function decaying at infinity, are not yet incorporated. To this end, we employ an envelope function [55], implemented in the log-domain for numerical stability. The log-envelope matrix has the form

$$\ln(e_{ij}) = - \left( x_i W_j^{(e)} \right)^2, \quad (18)$$

where  $i$  and  $j$  represent the index for the particle and the orbital, respectively, and  $W^{(e)} \in \mathbb{R}^A$  is the weight that is

learnt to determine the log-envelope of each orbital. We use gaussian envelopes, instead of the exponential ones of Ref. [12], which are closer to the non-interacting solution of Eq. (4).

We then take an element-wise product of  $M$  with the corresponding envelope,

$$\phi_{ij} = M_{ij} e_{ij}, \quad (19)$$

which yields a GSM. Each element of this matrix,  $\phi_{ij} = \phi_j(x_i; \{x_{/i}\})$ , may be understood as a generalised single-particle orbital on state  $j$ . This orbital does not only depend on the position of the particle  $i$ , but also on the positions of other particles in a permutation-invariant way, as indicated by the notation  $\{x_{/i}\}$  [12]. This has the significant benefit of making all orbitals depend on *all* particle positions, which amounts to an efficient encoding of backflow correlations in the wavefunction [12, 56].

Finally, we take the determinant of the GSM  $\phi$  to obtain an antisymmetric wavefunction. This is generically referred to as a generalised Slater determinant (GSD). In principle, a single GSD is sufficient to represent any antisymmetric wavefunction [57]. Empirically, we observe that one GSD captures nearly all the correlations in this system [26]. We note that the GSD is computed within the log-domain via a LU-decomposition. This choice is dictated by numerical stability.

Our computational framework is general, and we can modify both  $L$  and  $H$  if necessary. In the results shown here, we use  $L = 2$  equivariant layers of  $H = 64$  hidden nodes each, which show optimal results [26]. Details on the dependence of the results on  $L$  and  $H$  can be found in Ref. [26]. Our code can also work with more than one GSM and GSDs. If we were to employ  $d$  GSDs to describe the system, each determinant would have its own envelope through a  $d$  dependence of the envelope weights  $W^{(e)}$  in Eq. (18) [26]. In the  $d > 1$  case, the GSDs are summed via a signed-log-sum-exp function. We direct the reader to Appendix A of Ref. [26] for a complete and detailed explanation of the numerical implementation in the  $d > 1$  case.

Our approach is different to previous ML implementations [12, 27–29] in different ways. We drop the convolution layers, omit any accommodation of spin dependency, use gaussian envelopes instead of exponential ones, and work with improved numerical stability on the sum of GSDs. Crucially, we also do not incorporate any explicit Jastrow factor. This does not hamper the quality of the corresponding wave function, as we shall see below.

## 2. Variational Monte Carlo

Having defined the NQS ansatz, we now turn to discussing the details of how we implement a quantum many-body solution to our problem. We solve the Schrödinger equation via a VMC approach in two phases: a *pre-training* to an initial target wavefunction, and an *energy minimisation* to the unknown ground-state wavefunction.

The pre-training step can be thought of as a supervised learning exercise, where we demand that the network reproduces the many-body wave function of the non-interacting system. The idea is to obtain an initial state that is physical and somewhat similar, in terms of spatial extent, to the result after interactions are switched on. To do so, we minimise the loss,

$$\mathcal{L}^{Pre}(\theta) = \int dx_1 \dots dx_A |\Psi_\theta(x_1, \dots, x_A)|^2 \times \sum_{ij} [\phi_i(x_j; \{x_{/j}\}) - \varphi_i(x_j)]^2,$$

where  $\phi_i(x_j; \{x_{/j}\})$  is an element of the GSM and  $\varphi_i$  is the  $i^{\text{th}}$  HO single-particle state, see Eq. (3). The loss can be reformulated via MC sampling as

$$\mathcal{L}^{Pre}(\theta) = \mathbb{E}_{X \sim |\Psi_\theta|^2} \left[ \sum_{ij} [\phi_i(x_j; \{x_{/j}\}) - \varphi_i(x_j)]^2 \right], \quad (20)$$

where we define  $X = (x_1, \dots, x_A)$  as an  $A$ -dimensional random variable (or walker) distributed according to the Born probability of the many-body wavefunction,  $|\Psi_\theta|^2$ .

Initially, a set of  $N_W = 4096$  walkers are independently distributed at the origin of configuration space using a zero-mean and unit variance  $A$ -dimensional Gaussian distribution. The pre-training phase is then iterated for  $10^4$  epochs. Each epoch has three different phases. First, the  $N_W$  walkers are distributed in proportion to the Born probability of the NQS via a Metropolis-Hastings (MH) algorithm [58, 59]. We run 10 iterations of the MH algorithm per epoch. Second, we compute the local loss values and back-propagate to evaluate the gradients of the loss in Eq. (20) with respect to the parameters  $\theta$ . Third, we update the parameters using the Adam optimizer of Ref. [60], with default hyperparameters. Once the pre-training is complete, the NQS represents an approximate solution to the non-interacting case.

The next stage of our VMC approach is to minimize the expectation value of the energy to find the ground-state wavefunction, in a reinforcement learning setting. Using standard quantum Monte Carlo notation, the expectation value of the energy is formulated as a statistical average over *local* energies,

$$E = \frac{\langle \Psi_\theta | \hat{H} | \Psi_\theta \rangle}{\langle \Psi_\theta | \Psi_\theta \rangle} = \mathbb{E}_{X \sim |\Psi_\theta|^2} [\Psi_\theta(X)^{-1} \hat{H} \Psi_\theta(X)] \quad (21)$$

Within statistical uncertainties, this expectation value abides by the variational principle and  $E$  is larger than the ground state energy,  $E_{\text{g.s.}}$ .

We compute the kinetic energy in the log domain, which

leads to a local energy

$$E_L(X) \equiv \Psi_\theta(X)^{-1} \hat{H} \Psi_\theta(X)$$

$$= -\frac{1}{2} \sum_{i=1}^A \left[ \frac{\partial^2 \log |\Psi_\theta|}{\partial x_i^2} \Big|_X + \left( \frac{\partial \log |\Psi_\theta|}{\partial x_i} \right)^2 \Big|_X \right]$$

$$+ \sum_{i=1}^A \frac{x_i^2}{2} + \frac{V_0}{\sqrt{2\pi\sigma_0}} \sum_{i < j} e^{-\frac{(x_i - x_j)^2}{2\sigma_0^2}}. \quad (22)$$

The walkers are propagated using a MH algorithm. With this stochastic process, walkers can sample the arbitrary probability distribution dictated by the wavefunction Born probability. The process, however, may result in an autocorrelation in the calculation of many-body observables. To mitigate autocorrelation, we thin the Markov chain by propagating the chain 10 MH iterations between measurements of the local energies. Furthermore, we follow the methodology of Ref. [16] to adapt on the fly the width of the proposal distribution in the MH sampler. The aim is to ensure that, on average, approximately 50% of the walkers accept the proposed configuration at each step of the MH-algorithm. This allows for the proposal distribution to effectively scale with the system size, leading to a more efficient thermalization of the Markov chain.

For the sake of numerical stability, we follow Ref. [12] and use an  $\ell_1$ -norm clipping, in which we calculate a window of ‘acceptable’ local-energy values. We choose an  $\ell_1$ -norm as it is more robust to outliers. For a batch of local energies, we compute an average local energy,  $\langle E_L \rangle$ , with an associated  $\ell_1$ -norm. We define a window in the range  $\langle E_L \rangle \pm 5\ell_1$  and any values outside the window are replaced by the maximally accepted value in each side.

Once the expectation value of the energy is computed, we update the parameters of our ansatz using gradients with respect to  $\theta$ . We compute the gradients of the energy with reverse-mode AD via an auxiliary loss function,

$$\mathcal{L}(\theta) = 2\mathbb{E}_{x \sim |\Psi_\theta|^2} \left[ \perp \left( E_L - \mathbb{E}_{x \sim |\Psi_\theta|^2} [E_L] \right) \log |\Psi_\theta| \right], \quad (23)$$

where  $\perp(\dots)$  denotes the detach function [61]. This is a commonly used ML function, defined as equivalent to the identity function except that its derivative equals 0, i.e.  $\perp(x) = x$  but  $\frac{\partial \perp(x)}{\partial x} = 0$ . Whilst the expectation value of Eq. (23) does not equal the loss in Eq. (21), the derivatives of both expressions with respect to the parameters of the NQS are equal. The motivation for this loss function over the naïve implementation of Eq. (23) is numerical stability, as it allows for a calculation avoiding higher-order derivatives. One can prove that, by exploiting the detach function, the highest-ordered derivative that is required to compute the gradient is the second-order derivative with respect to  $x$  for the kinetic energy. A naïve implementation of gradients in Eq. (21) would have led to a third-order mixed derivative instead.

Just as in the pretraining phase, we use  $N_W = 4096$  walkers and minimize the energy for  $10^5$  epochs, including

10 MH sampling steps; computing local energies through Eq. (22); and back-propagating energy gradients in order to converge the NQS to the ground-state wavefunction. The parameters are updated using the Adam optimizer with default hyperparameters [60]. We show in Fig. 2 the evolution of the energy for one of the minimisation runs, for  $A = 6$ ,  $V_0 = -20$  and  $\sigma_0 = 0.5$ . This represents one of the more challenging cases presented here, with a relatively large number of particles and a strong deviation from the non-interacting case. We show both the central value of  $E$  (solid line) and the MC standard deviation of the integral of Eq. (21). We find that in about 10,000 epochs the energy is within 1% of the final value. The energy converges towards the ground state steadily, with relatively small oscillations around a central value (see inset).

We assume that the NQS reaches the ground state after  $10^5$  epochs and freeze the parameters,  $\theta$ , at that stage. To compute a final estimate of the energy, we follow Ref. [62] and calculate it over multiple batches via the ‘blocking’ method. We use  $10^4$  batches of 4096 walkers each, for a total of  $\approx 4.1 \times 10^7$  samples. We remove the aforementioned  $\ell_1$ -norm clipping, so as to not bias the final energy measurement. The final energy (and its standard deviation) is taken by averaging over these measurements. The total standard deviation is obtained by employing the implementation of the blocking method in Ref. [62]. The standard deviation of an individual chain is defined as,

$$\sigma_B^2 = \sigma^2 / (L_B / N_{corr}), \quad (24)$$

with  $\sigma_B$  and  $\sigma$  being the empirical standard deviation of a block,  $B$ , and of all samples, respectively.  $L_B$  is the length of a given block  $B$ , with correlation length  $N_{corr}$ . This standard deviation is usually extremely small and does not affect our conclusions.

All the observables throughout this paper are computed with this super-set of samples, which allows for sufficiently accurate measurements. More details on the implementation of NQS can be found in Ref. [26] as well as the GitHub repository [63].

### 3. Scaling with particle number

We now briefly comment on the scaling of the NQS method with the particle number. In our NQS, the number of weights is fixed for a given  $A$ , and we share collective particle features, such as the mean particle position  $\mu^{(0)}$ , over  $A$ -dependent embeddings. One main benefit of this equivariant embedding is its weight-sharing ability. The number of parameters for the equivariant layers (yellow areas in Fig 1) is independent of the number of particles, and has a quadratic dependence on the number of hidden nodes  $H$ . The particle number plays a role in the linear layer generating the GSM (beige area in Fig. 1), which has a dimension  $A \times (H + 1)$ , and thus scales linearly with  $A$ . The log-envelope layer also scales linearly with

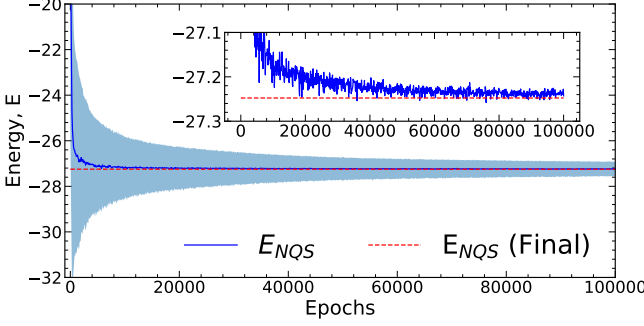


FIG. 2. The convergence of the expectation value of the energy for the  $A = 6$  system with  $V_0 = -20$  and  $\sigma_0 = 0.5$ , as a function of the epoch. The NQS ansatz is shown as a blue solid line. The standard deviation of the MC energy integral is shown with a shaded blue region. The final energy of the NQS, calculated via the blocking method, is shown in the red dashed line. For clarity, we show every 100<sup>th</sup> epoch in the convergence and omit the error bands in the inset.

particle number, to accommodate the asymptotics of each orbital. In total, the number of parameters has a linear dependence on  $A$  and a steeper quadratic dependence on  $H$ .

In practice, the number of parameters does not change substantially in going from  $A = 2$  to 6 for a fixed  $H$  dimension. In our case, with  $H = 64$  and  $L = 2$ , the  $A = 2$  NQS has 8580 parameters. In contrast, the  $A = 6$  NQS only has a total of 8844 parameters, a minute 3% increase. There may be a limit to the expressibility of the NQS when  $A$  is of the same order as  $H$ , but this can potentially be remedied by increasing  $H$ .

In addition to the dimensions of the weight matrices, the cost of the energy minimisation problem may be an issue. We find that the increase of walltime per epoch with  $A$  for our NQS is relatively small for the system sizes studied. We run all our experiments on a single P4000 Quadro GPU. In the  $A = 2$  case, the walltime is approximately 0.1 s per epoch, whereas it raises to 0.3 s per epoch in the  $A = 6$  case. The walltime may be significantly sped up with hardware improvements.

### B. Direct diagonalisation

We have employed a direct diagonalisation (or configuration interaction) method to provide a benchmark for the  $A$ -body NQSs. Specifically, we use the HO as the single-particle basis. We express the Hamiltonian of Eq. (2) in second quantization,

$$\hat{H} = \sum_{\alpha=1}^A \hat{n}_\alpha \epsilon_\alpha + \frac{1}{2} \sum_{\alpha, \beta, \gamma, \delta} V_{\alpha\beta, \delta\gamma} \hat{a}_\alpha^\dagger \hat{a}_\beta^\dagger \hat{a}_\gamma \hat{a}_\delta, \quad (25)$$

where  $V_{\alpha\beta, \delta\gamma}$  is the matrix element in the single-particle HO basis, with an analytical expression given in Ref. [64].  $\hat{n}_\alpha = \hat{a}_\alpha^\dagger \hat{a}_\alpha$  is the number operator, and  $\hat{a}_\alpha^\dagger$  ( $\hat{a}_\alpha$ ) are the

fermionic creation (annihilation) operators of the HO state  $\alpha$ .

In our implementation, we truncate the basis according to the many-body non-interacting energy, which also defines a single-particle basis truncation. In our calculations, we consider only the first  $N_{\max} = 20$  single-particle HO modes for all particle numbers. Having created the many-body basis, we then construct the Hamiltonian matrix and diagonalize it using the standard Lanczos algorithm. For details of this method, please refer to [44, 65].

Our calculations are limited by the basis truncation  $N_{\max}$ , which means that the results obtained through diagonalisation are not exact and can only provide upper-bound energies. Using a larger basis would lead to better results, but the many-body basis dimension scales exponentially with the number of particles, making it impractical for large systems.

As a consequence of using the HO basis, we obtain less error in the energy calculation for the repulsive interaction regime than for an attractive interaction. As we shall see below, this can be understood in terms of the spatial rearrangement of the system. However, as the number of particles increases even without changing the single-particle basis, the accuracy of the results diminishes. In this article, we have only considered the ground state, but we stress that this method also provides predictions for excited states.

### C. Hartree-Fock

We provide an additional benchmark by looking at the HF ground state, which is a minimal uncorrelated ansatz for the many-body wavefunction. We solve the problem in coordinate space, in keeping with the NQS implementation. This representation is particularly useful in capturing the relatively large changes in shape of the density distribution, which may otherwise be hard to describe with fixed-basis approaches.

The HF orbitals  $\phi_\alpha(x)$  with  $\alpha = 0, \dots, A - 1$  are fully occupied, with occupation numbers  $n_\alpha = 1$ . All the remaining states with  $\alpha \geq A$  are empty,  $n_\alpha = 0$ . The HF orbitals are used to construct a one-body density matrix,

$$\rho^{\text{HF}}(x'_1, x_1) = \sum_{\alpha=1}^A \phi_\alpha^*(x'_1) \phi_\alpha(x_1), \quad (26)$$

and the corresponding density profile  $n^{\text{HF}}(x) = \rho^{\text{HF}}(x_1 = x, x'_1 = x)$ . The orbitals are obtained from the HF equations,

$$\left[ -\frac{1}{2} \nabla^2 + \frac{1}{2} x^2 \right] \phi_\alpha(x) + \int d\bar{x} \Sigma(x, \bar{x}) \phi_\alpha(\bar{x}) = \varepsilon_\alpha^{\text{HF}} \phi_\alpha(x). \quad (27)$$

In the case of a finite-range interaction, the HF equations are a set of  $A$  integro-differential equations. The HF self-energy is the sum of a direct and a (non-local) exchange

term,

$$\begin{aligned}\Sigma(x'_1, x_1) = & \delta(x_1 - x'_1) \int dx V(x_1 - x) n^{\text{HF}}(x) \\ & + V(x'_1 - x_1) \rho^{\text{HF}}(x'_1, x_1).\end{aligned}\quad (28)$$

The corresponding HF energy is computed from the sum of single-particle energies and, as a consistency check, it can also be obtained from the direct integral of the mean-field, with the associated antisymmetry corrections [66].

We solve this set of self-consistent equations by iteration on a discretised mesh of equidistant points. The kinetic term is represented as a matrix using the Fourier grid Hamiltonian method [67], which works so long as the mesh extends well beyond the support of the wavefunctions. The mean-field can be computed efficiently with matrix operations, and Eq. (27) is reduced to an eigenvalue problem. We typically employ  $N = 200$  grid points extending from  $x = -5$  to 5 for small systems. For systems with  $A > 4$ , which have larger sizes, the mesh limits are extended to  $\pm 6$  and we choose  $N = 240$  points to keep the same mesh spacing. A computational notebook for the solution of the HF equations is available in Ref. [68].

#### D. Real-space solution for $A = 2$

In the following section, we use the  $A = 2$  system to determine which values of interaction strength and range are interesting. We have exploited two more numerical methods to solve specifically this problem.

For  $A = 2$  particles, the Hamiltonian in Eq. (1) is particularly easy to handle. Following Refs. [37, 69], we introduce a center of mass (CoM),  $R = \frac{1}{\sqrt{2}}(x_1 + x_2)$ , and relative coordinate,  $r = \frac{1}{\sqrt{2}}(x_1 - x_2)$ . With these, the Hamiltonian  $\hat{H} = \hat{H}_{\text{CM}} + \hat{H}_{\text{rel}}$  separates into two commuting components,

$$\hat{H}_{\text{CM}} = -\frac{1}{2}\nabla_R^2 + \frac{1}{2}R^2, \quad (29)$$

$$\hat{H}_{\text{r}} = -\frac{1}{2}\nabla_r^2 + \frac{1}{2}r^2 + \frac{V_0}{\sqrt{2\pi}\sigma_0}e^{-\frac{r^2}{\sigma_0^2}}. \quad (30)$$

The center-of-mass component is just an HO. The relative Hamiltonian includes an HO as well as the Gaussian interaction component. We note that the gaussian in relative coordinates has a different width and it is effectively wider than the original interaction.

The CoM and relative Hamiltonians can be diagonalized separately, providing eigenstates  $\varphi_\alpha(R)$  and  $\psi_\beta(r)$  with eigenenergies  $\epsilon_\alpha$  and  $\epsilon_\beta$ , respectively. For the relative coordinate, we need to solve the eigenvalue problem

$$\left[ -\frac{1}{2}\nabla_r^2 + \frac{1}{2}r^2 + \frac{V_0}{\sqrt{2\pi}\sigma_0}e^{-\frac{r^2}{\sigma_0^2}} \right] \psi_\beta(r) = \epsilon_\beta \psi_\beta(r). \quad (31)$$

Because of the Pauli principle, the only acceptable solutions are those that are antisymmetric in the relative

coordinate,  $\psi_\beta(-r) = -\psi_\beta(r)$ . These correspond to odd values of  $\beta$ , and hence the ground state will necessarily correspond to  $\beta = 1$  rather than lowest-energy, space-symmetric  $\beta = 0$  state. To solve this problem numerically, we discretize the relative coordinate in an evenly spaced mesh. As in the HF case, the kinetic term is discretized as a matrix using the Fourier grid Hamiltonian method [67]. We employ  $N = 200$  grid points extending from  $r = -5$  to 5. A computational notebook for this problem is also available in Ref. [68].

If a numerical solution to  $\psi_\beta$  is available, the total two-body wavefunction is the product,

$$\Psi_{\alpha,\beta}(x_1, x_2) = \varphi_\alpha\left(\frac{1}{\sqrt{2}}(x_1 + x_2)\right) \times \psi_\beta\left(\frac{1}{\sqrt{2}}(x_1 - x_2)\right). \quad (32)$$

The total energy of the ground state is given by  $E = \epsilon_0 + \epsilon_1 = \frac{1}{2} + \epsilon_1$ . We only discuss the ground state of the system, but note that this method can also provide the rest of the spectrum for  $A = 2$ .

#### E. Perturbation theory for $A = 2$

Alternatively, one can solve for the energy  $\epsilon_\beta$  using standard perturbation theory tools. We take the HO as a reference state, so that  $\psi_\alpha^{(0)} = \varphi_\alpha$  and  $\epsilon_\alpha^{(0)} = \epsilon_\alpha$ , where  $\varphi_\alpha$  and  $\epsilon_\alpha$  are HO eigenstates and eigenvalues. The gaussian interaction term is then treated as a perturbation. We employ known analytical expressions for the matrix elements  $V_{\alpha\beta} = \frac{V_0}{\sqrt{2\pi}\sigma_0} \left\langle \varphi_\alpha \left| e^{-\frac{r^2}{\sigma_0^2}} \right| \varphi_\beta \right\rangle$  [70]. The zero-order results are just the eigenvalues of the non-interacting confined two-particle system, Eq. (5), which in the ground state yields  $E^{(0)} = 2$ . Noting that antisymmetry constraints force  $\alpha$  and  $\beta$  to take odd values, we find that the first order perturbation theory (PT1) expression for the total energy is,

$$E^{(1)} = E^{(0)} + V_{11} = 2 + \frac{V_0}{\sqrt{2\pi}} \frac{\sigma_0^2}{(1 + \sigma_0^2)^{3/2}}. \quad (33)$$

As expected, this expression is linear in the perturbation strength  $V_0$ . The slope of the energy dependence on  $V_0$  is dictated by  $\sigma_0$ . For small values of  $\sigma_0$ , the slope grows quadratically. In other words, the departure from the non-interacting case is quadratic in  $\sigma_0$ . For large values of  $\sigma_0$ , in contrast, the slope decreases like  $1/\sigma_0$ . This is to be expected since, by construction, the parametrization of our interaction term has such a  $1/\sigma_0$  dependence.

Second (PT2) and third (PT3) order perturbation theory results can be readily obtained from the corresponding matrix elements  $V_{\alpha\beta}$ . We use up to 8 additional states in the intermediate sums, which provide are already converged for all practical purposes. We provide a computational notebook in Ref. [68]. As we shall see below, these PT estimates allow us to find regions of parameter space where non-perturbative effects are particularly important.

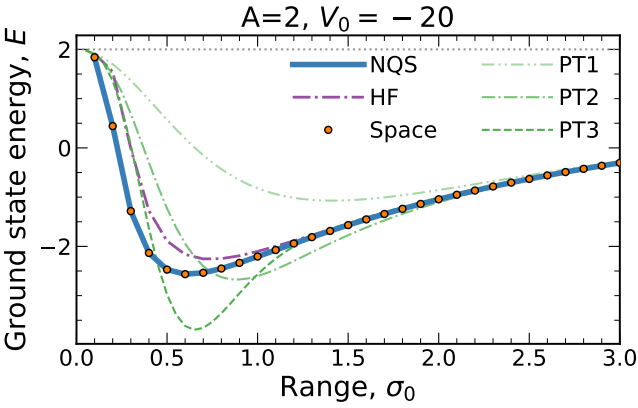


FIG. 3. The ground state energy of the  $A = 2$  system as a function of the range,  $\sigma_0$ , for a large and attractive interaction strength,  $V_0 = -20$ . The NQS ansatz energy for  $H = 64$ ,  $L = 2$ , and  $D = 1$  is shown as a solid line. The orange circles represent the real-space solution. The short-dash-dotted purple line is the Hartree-Fock solution. The double-dotted-dashed, dotted-dashed, and dashed green lines show the perturbation theory results to first (PT1), second (PT2), and third orders (PT3), respectively. The horizontal dotted line is the non-interacting energy baseline.

#### IV. RESULTS

In this section, we show the results obtained for spinless fermionic systems from  $A = 2$  to  $A = 6$  with different methods. We start with a discussion of the two-body case in the first subsection. This allows us to perform an exploration of the dependence of the results in  $V_0$  and  $\sigma_0$ . Results for  $A > 2$  are discussed in the following subsection.

##### A. Two-body sector

The two-body case is already relatively complicated. The solution for a zero-range interaction is well known [69], and semianalytic solutions for specific finite-range interactions are also available [37].

###### 1. Energy

The dependence on  $V_0$  and  $\sigma_0$  of the energy of the  $A = 2$  mimicks that of heavier systems. We are particularly interested in finding regions of non-perturbative behaviour, to test the performance of the NQS ansatz in the most challenging scenarios. We start by looking at the dependence on the range of the interaction,  $\sigma_0$ . We note that our pursuit here is mostly theoretical and that the values of interaction range and strength that we explore may not be directly accessible by near-term experiments.

We start by considering a very attractive interaction, with  $V_0 = -20$ . The results for the ground state energy

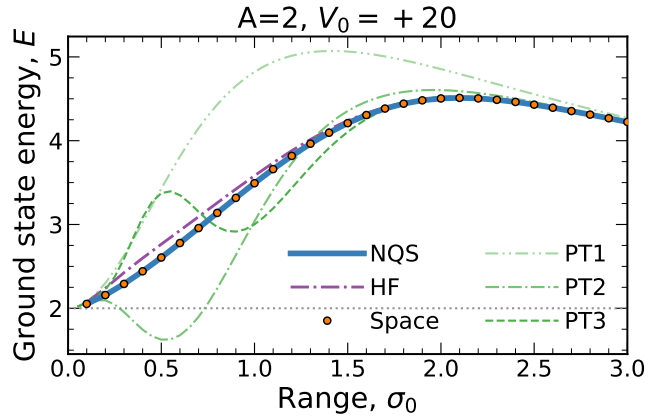


FIG. 4. The same as Fig. 3 but for a large and repulsive interaction strength,  $V_0 = +20$ .

are shown in Fig. 3. In this plot, we show the NQS ansatz with a solid line, which includes the statistical VMC uncertainty that is typically smaller than  $10^{-5}$  in the same units. We also show the HF (short-dashed-dotted purple line) and the real-space (filled circles) solutions. To analyse how perturbative the results are, we also display the PT1, PT2 and PT3 predictions for the energy with different linestyles.

For  $A = 2$  particles, the non-interacting case corresponds to  $E = 2$ , shown in the figure as a horizontal dotted line. As expected, all the methods agree with this value as the range tends to zero,  $\sigma_0 \rightarrow 0$ . As a function of the range, all energy predictions subsequently decrease, reach a model-dependent minimum value and eventually increase to reach an asymptotic  $\sigma_0^{-1}$  behaviour.

The comparison between different methods provides an insight on the complexity of the problem. First, we note that the NQS solution agrees perfectly well with the real-space solution along a wide range of values. The minimum of energy as a function of  $\sigma_0$  lies around  $\sigma_0 \approx 0.5$  and yields  $E \approx -2$  for this particular value of  $V_0$ . We conclude that the network is performing well across a wide range of values of  $\sigma_0$ .

The NQS outperforms variationally the HF solution across a wide range of values. In particular, the HF solution has a somewhat shallower minimum at a larger value of  $\sigma_0$ . Note that the HF prediction is the optimal solution for a Slater determinant formed of single-particle orbitals  $\phi_\alpha(x)$  [53, 71]. The HF single-particle orbitals depend on a single position. The NQS outperforms this solution by exploiting backflow correlation in the generalized orbitals of the GSM. These orbitals depend both on  $x_1$  and  $x_2$  through the equivariant embedding.

The convergence of the perturbation theory results provides an indication of the “perturbativeness” of the two-body problem. The PT1 (dashed-double-dotted line) result of Eq. (33) is far too repulsive across all values of the range. It only gets close to the NQS and real-space results well beyond its shallow minimum, which happens

at  $\sigma_0 = \sqrt{2}$ . The PT2 results for small values of  $\sigma_0$  are substantially closer to the NQS ones, but they cannot reproduce the correct dependence with  $\sigma_0$  below about  $\sigma_0 \approx 2$ . In contrast to the PT1 prediction, the PT2 result is more attractive than the NQS prediction beyond about  $\sigma_0 \approx 0.7$ . Something similar happens with PT3, which is well below the NQS solution from  $\sigma_0 \approx 0.5$  onwards. We find that these third-order results are still rather far from the true values and, in particular, the convergence pattern is relatively erratic for values between  $\sigma \in [0.5-0.9]$ . This challenging region in parameter space may be a good test bed for the NQS solution.

We confirm that this region of ranges is particularly non-perturbative by looking at a very repulsive case. We show in Fig. 4 the predictions for the ground state energy of the  $A = 2$  system for a value of  $V_0 = +20$ . The shape of the energy predictions here is substantially different. The NQS energy departs from the non-interacting baseline at  $\sigma_0 = 0$ , and increases to a maximum of around  $E \approx 4$  at  $\sigma_0 = 2$ . Just as in the attractive case, large values of the range lead to relatively perturbative results, in the sense that PT1, PT2 and PT3 predictions agree with the exact benchmarks. In contrast, for values of the range below  $\sigma_0 = 1$  the PT predictions follow a complex pattern. In particular, the PT2 and PT3 results show anomalous oscillations around  $\sigma_0 = 0.5$ . All in all, we conclude that for values of interaction strength of the order of  $V_0 \approx \pm 20$ , non-perturbative behaviours occur for interaction ranges of the order of  $\sigma_0 = 0.5$ . While we do not show them for brevity here, we stress that the dependence of the NQS and HF energies on the range  $\sigma_0$  for systems with  $A > 2$  has a very similar behaviour to those shown in Figs. 3 and 4. The interested reader can find this information in Ref. [26].

The analysis of the  $\sigma_0$  dependence of our results leads us to conclude that a value of  $\sigma_0 = 0.5$  is well within the non-perturbative regime. We now explore the dependence of the ground state energy on the interaction strength,  $V_0$ , to analyze the performance of the NQS ansatz. The results for  $A = 2$  are shown in the three panels of Fig. 5. Panel (a) shows a comparison between the NQS ground state energy (solid lines) and the different PT results. This provides an idea of the perturbative nature of the system as a function of  $V_0$ , rather than  $\sigma_0$ . The PT1 prediction (dashed-double-dotted line) of Eq. (33) is, as expected, linear in  $V_0$  and captures the full dependence on  $V_0$  only for small values of  $V_0$ ,  $|V_0| < 4$ . PT2 results (dashed-dotted line) are valid in a wider strength range, but overpredict (underpredict) the true ground state energy at large negative (positive) values of  $V_0$ . PT3 results (short-dashed line) work well within a range  $-15 < V_0 < 10$ , but fail beyond this range. Again, this analysis indicates that the most attractive and repulsive values of  $V_0$  are in a non-perturbative regime.

We compare the NQS results to more realistic benchmarks in panel (b) of Fig. 5. Overall, we find an excellent agreement between the real-space solution and the NQS prediction. The direct diagonalisation result also provides a good energy prediction, although minor deviations with

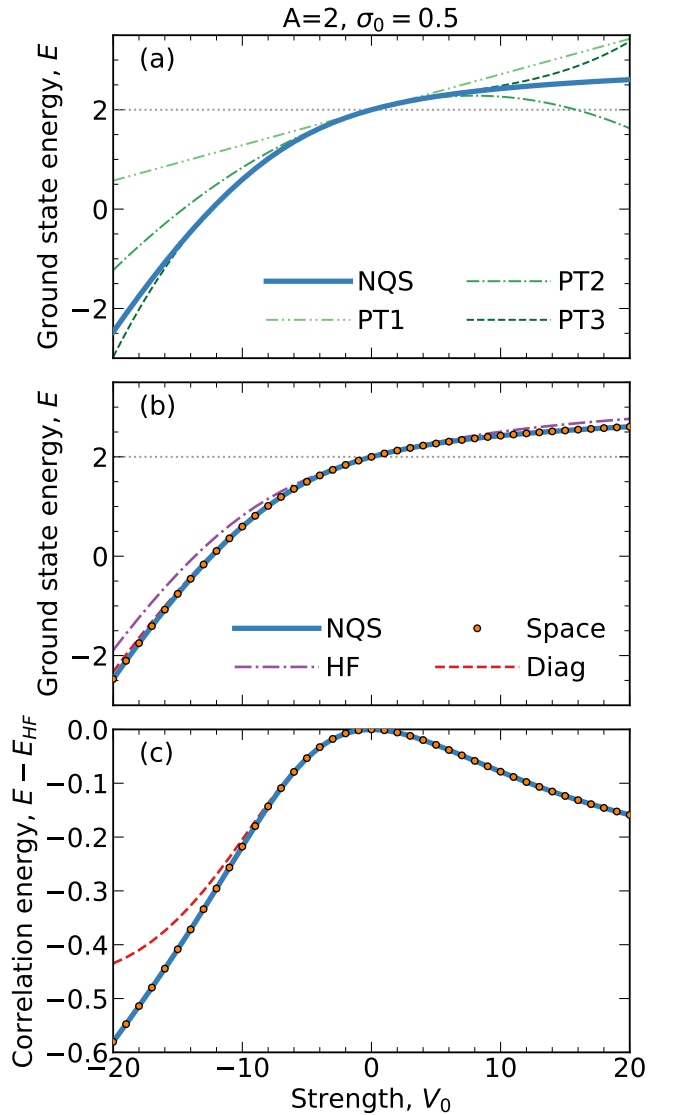


FIG. 5. Energy of the  $A = 2$  system as a function of interaction strength,  $V_0$ , for a fixed range,  $\sigma_0 = 0.5$ . Panel (a): comparison of the NQS ground state energy (solid line) to perturbation theory results. Panel (b): comparison of the NQS ground state energy (solid line) to the real-space solution of the  $A = 2$  system (filled circles); direct diagonalisation results (dashed red line); and the HF approximation (short-dashed-dotted purple line). Panel(c): NQS, real-space solution and direct diagonalisation predictions for the correlation energy,  $E_c = E - E_{HF}$ .

respect to the NQS are observed at large negative values of the coupling. The NQS provides better variational results than the HF approximation, thanks to the presence of backflow correlations.

We now comment on the overall dependence of the energy on  $V_0$ . In the non-interacting limit,  $V_0 = 0$ , all methods agree exactly with the baseline value,  $E = 2$ . In the repulsive side, as the interaction strength increases in magnitude, the energy generally increases above the

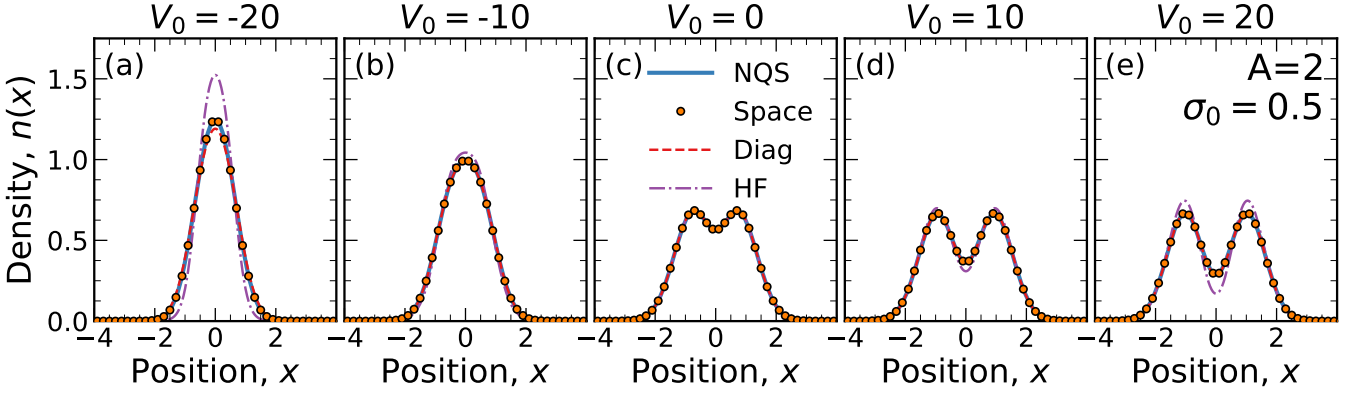


FIG. 6. The density profile  $n(x)$  of the  $A = 2$  system as a function of position  $x$ . Panels (a) to (e) show results for values of  $V_0$  from  $-20$  to  $20$  in steps of  $10$ . See Fig. 5 for an explanation of the legend.

baseline, and seems to saturate to a value that lies close to  $E \approx 2.5$ . On the attractive side, in contrast, the energy decreases relatively rapidly. At around  $V_0 \approx -10$ , the system energy becomes attractive. The total energy then decreases in absolute value as  $V_0$  becomes more and more attractive. It is immediately clear from the energetics of the system that the attractive and the repulsive regimes are very different from each other.

This difference becomes even more evident in panel (c), which shows the correlation energy of the system. We define this as the difference in ground state energy of a given method and the HF prediction,  $E_c = E - E_{\text{HF}}$ . The correlation energy departs from zero at  $V_0$ . In the repulsive side,  $E_c$  slowly increases in absolute magnitude. At  $V_0 = 20$ , we find  $E_c \approx -0.15$ , which is about 6% of the total energy. In contrast, in the attractive regime, the NQS prediction is  $E_c \approx -0.6$ , which is a substantial contribution to the total energy of  $E \approx -2$  at that same value. There is no sign of saturation of the correlation energy in either side of  $V_0$ . We also note that the direct diagonalisation result departs from both the real-space and the NQS prediction for values of  $V_0 < -10$ . This discrepancy is due to the truncation of the model space, as we shall see next.

## 2. Density profile

To further understand the origin of the correlations of the system, we look at the density profile of the system,  $n(x)$ . Figure 6 shows the density profile obtained with the different many-body approaches for five different values of  $V_0$ , ranging from  $-20$  to  $20$  in steps of  $10$ . Panel (c) shows the non-interacting result,  $V_0 = 0$ . Here, all methods agree, as expected. The density profile has a well-understood dip at the center, due to the interplay between the  $n = 0$  and  $n = 1$  HO orbitals. These density modulations are typical in fermion systems [37]. Panels (d) and (e) show the same densities in the repulsive regime, at interaction values of  $V_0 = 10$  and  $20$ , respectively. We

find that the central dip of the density decreases, while the overall size of the density profile is relatively constant. We find a very clear agreement between the real space solution of the  $A = 2$  problem, the direct diagonalisation method and the NQS prediction. In contrast, the HF result seems to overestimate the fermionic structures, with a lower dip and higher density maxima. In other words, the HF orbitals appear to be more localized than their correlated counterparts.

Physically, the picture that arises in the repulsive regime is akin to that of (Wigner) crystallization [72–77]. As the inter-particle interaction strength increases, the system minimises the interaction energy by keeping particles beyond the interaction range. Doing so, however, comes at the price of increasing the potential energy due to the HO well. A similar difference in the localization patterns of HF and fully correlated predictions was observed in the 3D Wigner crystal of an electron gas [78].

In contrast, the density profile in the attractive regime, shown in panels (a) and (b) of Fig. 6, is characterized by a relatively featureless structure. The fermionic dip disappears around  $V_0 \approx -10$  and, for more attractive strength values, the density profile is a simple peak that narrows down and increases in height as  $V_0$  becomes more negative. In fact, a longstanding prediction in one-dimensional systems suggests that spinless fermionic systems with strongly attractive interactions should behave like non-interacting bosonic systems [31, 32, 35–38, 79–81]. The density profile for the  $A = 2$  system clearly supports this hypothesis. It is worth stressing that the NQS grasps the bosonization transition without any further adjustments. We also stress that our results are qualitatively similar to the semianalytical solution of Ref. [37], where a soft-core, square-well interaction was used.

## 3. Occupation numbers

The density profile  $n(x)$  is just a component of the OBDM. We can access the OBDM with the benchmark

methods discussed so far. With NQSs, we calculate  $\rho(x'_1, x_1)$  stochastically using the ghost-particle method of Ref. [82]. For the real-space solution, we perform the integral in Eq. (6) over the uniform mesh grid. The solution of Eq. (7) can then be easily obtained as a matrix diagonalisation problem in a spatially uniform grid. With the direct diagonalisation method, we calculate  $\rho$  in the second quantization formalism, with the definition

$$\rho_{\alpha\beta} = \langle \Psi | a_\alpha^\dagger a_\beta | \Psi \rangle, \quad (34)$$

where  $|\Psi\rangle$  is the precomputed ground-state wavefunction and  $\rho_{\alpha\beta}$  are the matrix elements of  $\rho$ . Finally, we diagonalise  $\rho$  to obtain the eigenvalues  $n_\alpha$  in the many-body basis.

Panel (a) of Fig. 7 shows the evolution of the occupation numbers for the  $A = 2$  systems as a function of interaction strength. We benchmark the NQS results (solid circles) to the real-space solution (empty circles) and the direct diagonalisation approach (dashed lines). We find an excellent agreement between all three methods. We note that we do not include a comparison to the HF benchmark, which provides a relatively good description of the energy of the system. For occupation numbers, however, the HF approach is limited to either fully occupied or fully unoccupied states and does not provide an accurate metric for one-body correlations.

For  $A = 2$ , there is a double degeneracy in the natural orbital occupations, which the NQS can handle seamlessly. The occupation values  $n_{\alpha \leq A}$  departs from 1 as the absolute value of  $V_0$  increases. We find that the rate of change is different depending on whether we are on the attractive or the repulsive side, a result that mimics the correlation energy displayed in panel (c) of Fig. 5. In the repulsive side, for  $V_0 = 20$ , the occupation is about  $\approx 96\%$ , indicating a relatively uncorrelated system. The tendency to deviate from 1 as  $V_0$  increases, however, indicates that even in the crystalline phase, particles are not entirely described by locally confined individual orbitals [37]. In contrast, in the attractive case, for  $V_0 \approx -20$  the occupation number is  $n_\alpha \approx 0.9$ . This suggests a stronger role of correlations in the bosonized phase.

Panel (b) shows a similar figure for ‘unoccupied’ orbitals,  $n_{\alpha \geq A}$ . The plot is given in logarithmic scale and includes the first 14 orbitals in the NQS diagonalisation. Due to the stochastic nature of the OBDM estimation in the NQS approach, there is a prominent statistical noise floor of the order of  $\approx 10^{-2}$ . While this limits some of the conclusions that can be drawn, we stress that the NQS many-body wavefunction is comparable (if not better) variationally than the other estimates. The values of  $n_\alpha$  above the statistical threshold should therefore provide a more faithful representation of the true occupation numbers.

Just as in Panel (a), we find that the repulsive and attractive sides are qualitatively different. On the repulsive side, we find a doubly-degenerate state with an increasing occupation that reaches values close to  $n_\alpha \approx 0.02 - 0.03$  for the most repulsive interaction strengths. On the attrac-

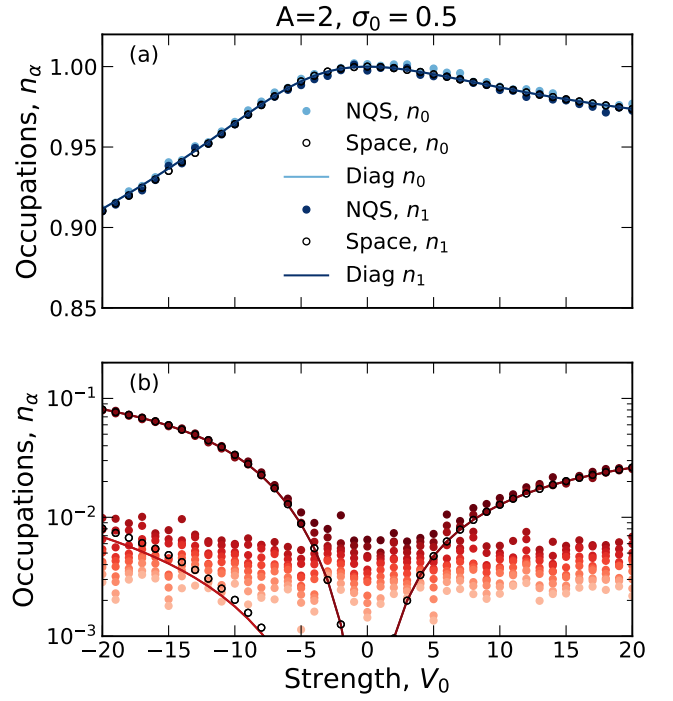


FIG. 7. Occupation probabilities for the  $A = 2$  system as a function of interaction strength for a fixed range  $\sigma_0 = 0.5$ . Panel (a) shows the occupations for the two hole states below the Fermi surface. Panel (b) shows (in logarithmic scale) the occupations of particle states. We compare the NQS results (solid circles) to real space results (empty circles). Solid lines correspond to the direct diagonalisation results.

tive side, in contrast, the equivalent doubly-degenerate eigenstate is significantly more occupied, reaching values of  $n_\alpha \approx 0.08$  for  $V_0 = -20$ . Both the real-space solution and the direct diagonalisation methods predict another doubly-degenerate eigenstate, with an occupation that is about 10 times smaller. The NQS cannot resolve this state, as it lies within its statistical floor. Overall, however, the picture reinforces the idea that correlations have a very different nature on the attractive and the repulsive side. A priori, it appears that the bosonized phase has a more complex structure, admixing more single-particle modes than the corresponding crystalline phase.

## B. Few-body sector

We now turn our discussion to the results obtained in the few-body sector, for systems with  $A = 3$  up to  $A = 6$  particles. We continue to benchmark NQS results against the direct diagonalisation approach as well as the HF method. The real-space solution is not available for  $A > 2$ . We advance that several of the physics conclusions we drew on the two-body system remain the same in the few-body domain.

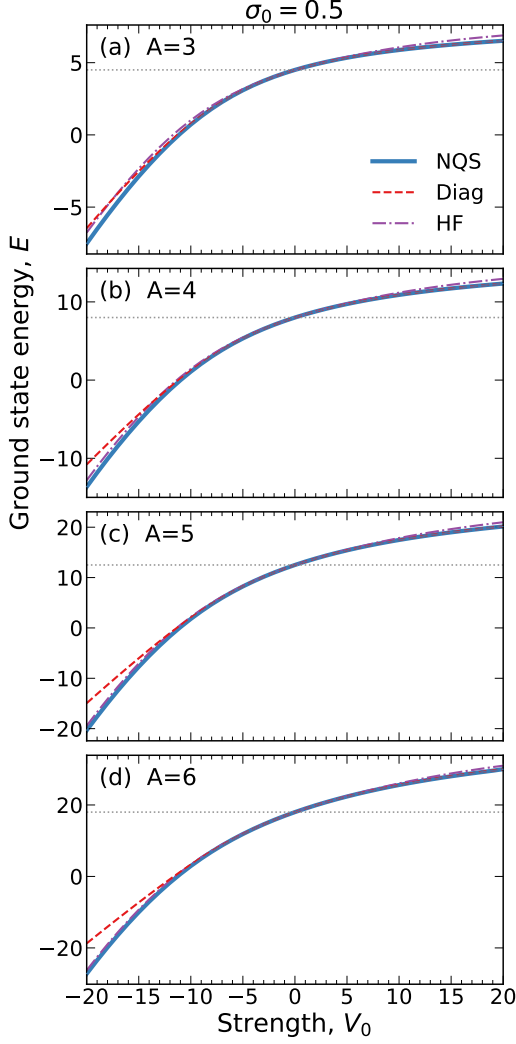


FIG. 8. The ground-state energy of the  $A$ -particle system as a function of interaction strength,  $V_0$ , for a fixed range,  $\sigma_0 = 0.5$ . Panels (a) to (d) correspond to systems of  $A = 3$  to  $A = 6$  particles. See Fig. 5 for an explanation of the legend.

### 1. Energy

We start by considering the energy of the system. Panels (a) to (d) in Fig. 8 show the energy for  $A = 3$  to 6 particles as a function of  $V_0$ . We focus on the case with a range value of  $\sigma_0 = 0.5$ . The qualitative behaviour of the energy in all these systems is very similar to that in the  $A = 2$  case. On the repulsive side, the system energy increases slowly and tends to plateau at a value which is about 1.25 – 1.6 times the non-interacting value. In this repulsive range, a power-law scaling with the particle number,  $E \approx A^{2.2}$ , approximates the complete results well. The saturation of the energy as  $V_0$  becomes more negative bodes well with the physical picture of a crystal. This picture is further reinforced by the density profiles, which we present later. In the attractive regime, in contrast, the energy per particle decreases much more steeply

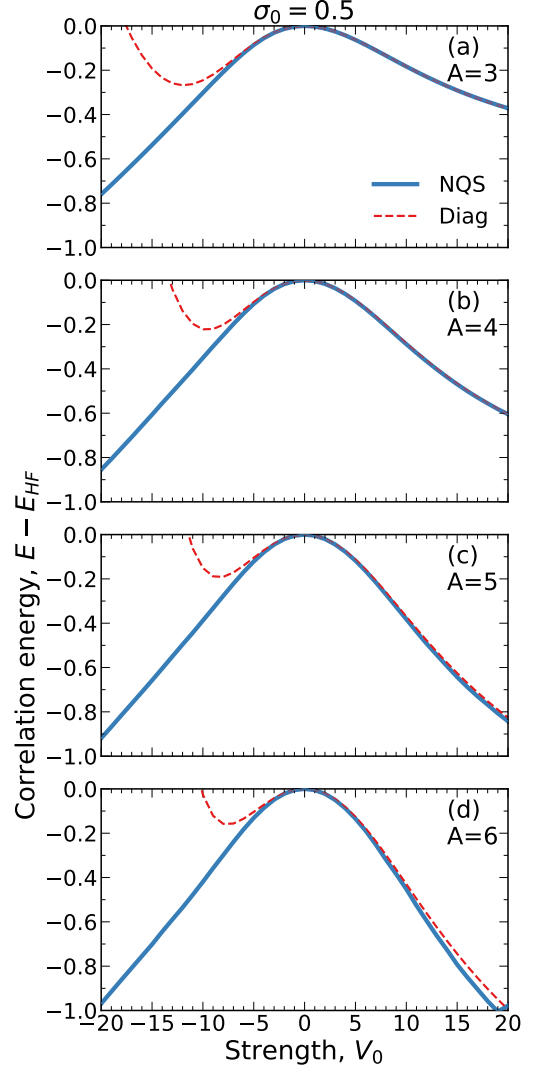


FIG. 9. The correlation energy of the  $A$ -particle system as a function of interaction strength,  $V_0$ , for a fixed range,  $\sigma_0 = 0.5$ . Panels (a) to (d) correspond to systems of  $A = 3$  to  $A = 6$  particles. See Fig. 5 for an explanation of the legend.

as a function of  $V_0$ , with no signs of saturation as  $V_0$  becomes more negative.

In terms of benchmarks, we notice two different remarkable tendencies. First, the HF results overestimate the ground-state energy, as expected. The difference between the HF and the NQS prediction becomes less noticeable as the particle number increases. In other words, the HF approximation becomes more reliable in relative energy terms as the number of particles increases. This is not so surprising, since the mean-field picture should work better as the number of particles increases. Second, we find that the exact diagonalisation technique is always less bound than the NQS prediction for values  $V_0 < -10$ . We interpret this as a sign that the size of the diagonalisation space becomes insufficient. In the bosonized regime, the density of the system is substantially more compressed

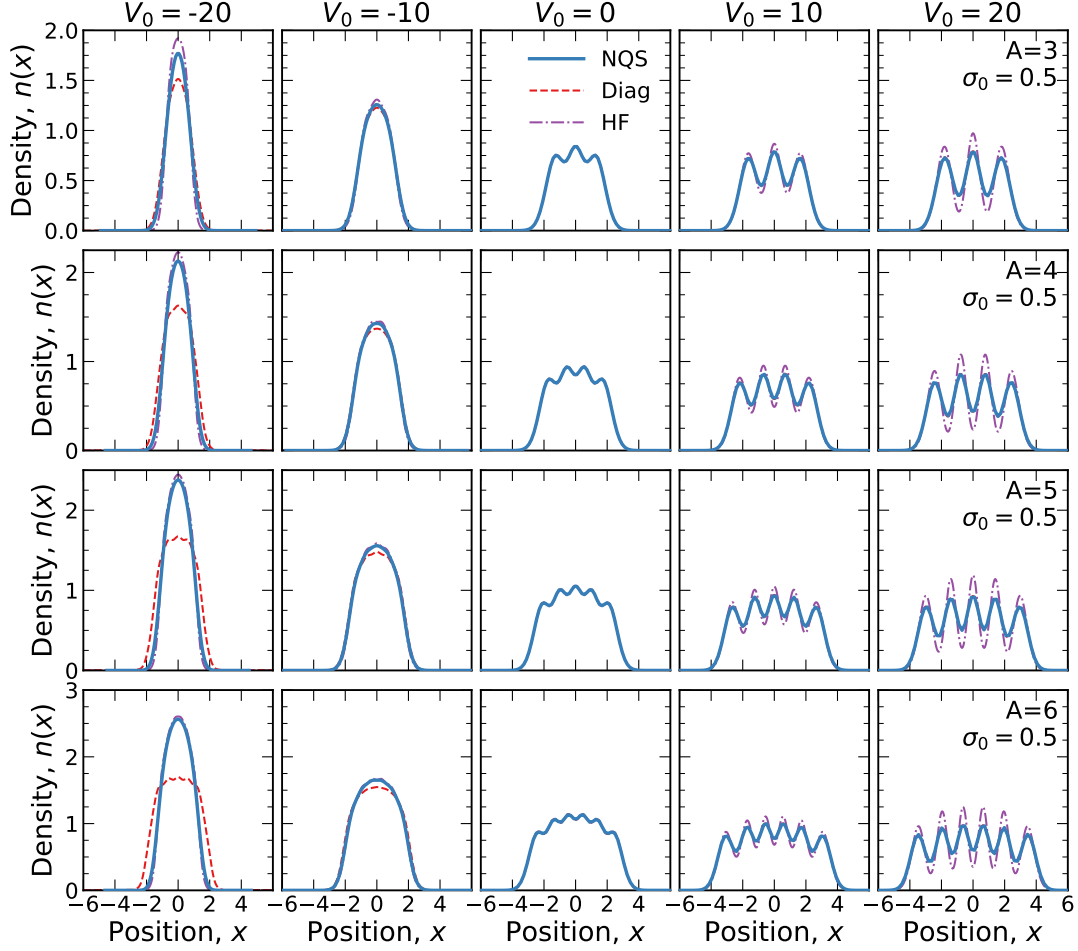


FIG. 10. Density profiles  $n(x)$  as a function of position  $x$  for different values of  $V_0$  and a fixed range  $\sigma_0 = 0.5$ . From left to right,  $V_0$  goes from  $-20$  to  $20$  in increments of  $10$  units. From top to bottom, we show the results for  $A = 3, 4, 5$  and  $6$  particles.

than the non-interacting HO case. One may thus expect to need many more single-particle modes to describe the density profile and the energetics of the system.

To quantify further the importance of correlations in the system, we look at the correlation energy for the  $A = 3$  to  $6$  particles as a function of  $V_0$  in Fig. 9. We stress that the energy scale is the same for all panels. In other words, the difference between the HF and the full result appears to be relatively constant independently of the particle number. On the repulsive regime at  $V_0 = 20$ , the energy increases by about  $0.2$  units every time that we add one more particle to the system. In contrast, the increase on the attractive side is less steep. In the attractive side, the direct diagonalisation approach yields a relatively poor description of the correlation energy. Non-physical, positive values of  $E_c$  are achieved for coupling constants below  $V_0 < -10$  or  $-15$ . On the repulsive side, we also find signs of a relatively poorer description of the correlation energy with the direct diagonalisation approach for  $A \approx 6$ . Having said that, it is clear that the direct diagonalisation approach works much better in the repulsive side, where deviations from the NQS prediction are within  $0.05$  in

absolute energy terms.

## 2. Density profiles

It is also very useful to inspect the density profiles,  $n(x)$ , of the systems with  $A = 3$  to  $6$  particles. We summarise these results in Fig. 10, where the columns correspond to different interaction strengths and the rows correspond to different numbers of particles. We compare predictions from the NQS, the direct diagonalisation approach and the HF approximation.

The middle panels, corresponding to the non-interacting case ( $V_0 = 0$ ), show  $A$  peaks on top of a Gaussian-like overall behaviour. This is an expected behaviour, which arises as a result of Eqs. (3) and (26). In the attractive regime, the peak-like fermionic structure in the density profile disappears from  $V_0 \approx -10$  onwards. The NQS results show a single peak, that becomes narrower as  $V_0$  becomes more attractive. This is in line with the HF prediction, which approaches the NQS result as the number of particles increases. In contrast, the exact

diagonalisation approach is unable to grasp the narrow density distribution beyond  $V_0 \leq -10$ . At  $V_0 = -20$ , the NQS and HF density distributions are almost a factor of 2 narrower than the non-interacting case. It is naively expected that the model space in the exact diagonalisation cannot capture such strong density rearrangements.

In the strongly repulsive limit,  $V_0 \gg 0$ , the interaction effectively separates the fermions apart, leading to the full crystallisation of the system [73, 76]. The separation of single-particle orbitals, however, cannot proceed indefinitely because the harmonic trap is more and more effective as  $|x|$  increases. While the position of the  $A$  density peaks barely changes, the troughs between them become more and more defined as  $V_0$  increases. In this repulsive regime, the direct diagonalisation results coincide with the NQS predictions for the density profile. In contrast, the HF approach fails substantially. The HF density profiles overestimate (underestimate) the peaks (troughs) and the disagreement becomes more pronounced as the number of particles increases. More details on the density profile and the average size of the system are provided in Ref. [26].

The difference of the density profiles in the attractive and repulsive regimes is reflected into the energetics of the system. We show different contributions to the total energy as a function of the interaction strength  $V_0$  in Fig. 11. Panels from top to bottom correspond to different numbers of particles, from  $A = 2$  (top) to  $A = 6$  (bottom). We distinguish the contributions due to the kinetic energy,  $\langle K \rangle = \langle \Psi | \sum_i -\frac{\partial_i^2}{2m} | \Psi \rangle / \langle \Psi | \Psi \rangle$ ; the (external) harmonic oscillator potential energy,  $\langle U \rangle = \langle \Psi | \sum_i -\frac{x_i^2}{2} | \Psi \rangle / \langle \Psi | \Psi \rangle$ ; and the interaction energy,  $\langle V \rangle = V_0 / (\sqrt{2\pi}\sigma_0) \langle \Psi | \sum_{i < j} e^{-(x_i^2 - x_j^2)/2\sigma_0^2} | \Psi \rangle / \langle \Psi | \Psi \rangle$ . These components are all computed stochastically using the NQS wavefunction probability.

We find a common picture, which is relatively independent of the particle number. In the non-interacting case, the virial theorem stipulates that  $\langle E \rangle = 2\langle K \rangle = 2\langle U \rangle$  (and  $\langle V \rangle = 0$ ). In the repulsive side, the harmonic oscillator and the interaction energy components increase very slowly as  $V_0$  grows. We interpret this slow growth in terms of localisation. When the single-particle orbitals become localised into  $A$  well-defined, equidistant peaks, the sharpening of the fermionic features only modifies these two components slightly. In contrast, the kinetic energy reduces substantially as a function of  $V_0$ . In fact, for particle numbers  $A > 4$ , we observe that  $\langle K \rangle \leq \langle V \rangle$ , a condition that is typically employed to characterise a (Wigner) crystal [76].

The analysis in terms of different energy components indicates that the energy in the attractive regime behaves rather differently. First of all, we find that the attractive total energy in the regime where  $V_0 \ll 0$  is the result of the cancellation of two large but opposite energy components. On the one hand, the kinetic energy  $\langle K \rangle$  increases substantially as  $V_0$  decreases, as a result of the strong density rearrangement. On the other, the interaction en-

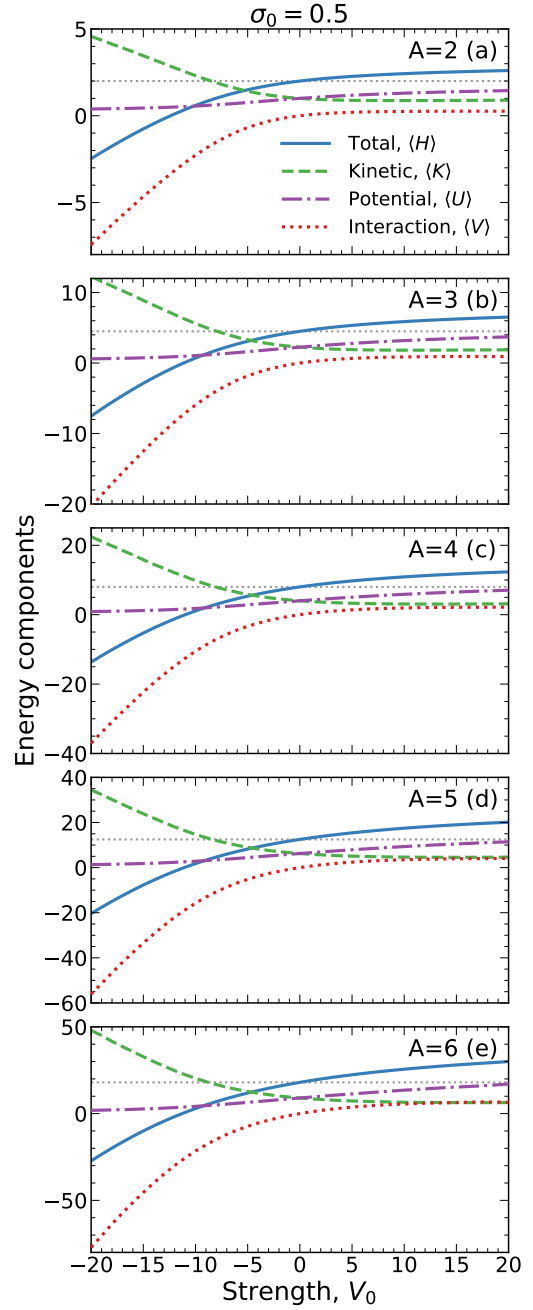


FIG. 11. Different components of the NQS ground state energy as a function of interaction strength,  $V_0$ , for a fixed range  $\sigma_0 = 0.5$ . Solid, dashed, dash-dotted and dotted lines correspond to the total, kinetic, harmonic oscillator and interaction energies, respectively. Panels (a) to (e) correspond to systems of  $A = 2$  to  $A = 6$  particles. The horizontal dotted line is the non-interacting ground-state energy.

ergy  $\langle V \rangle$  becomes extremely attractive as all the particles are confined near the center of the trap and, consequently, near each other. The central confinement also leads to a near cancellation of the harmonic oscillator potential energy  $\langle U \rangle$ .

At this stage, we can draw some conclusions about the

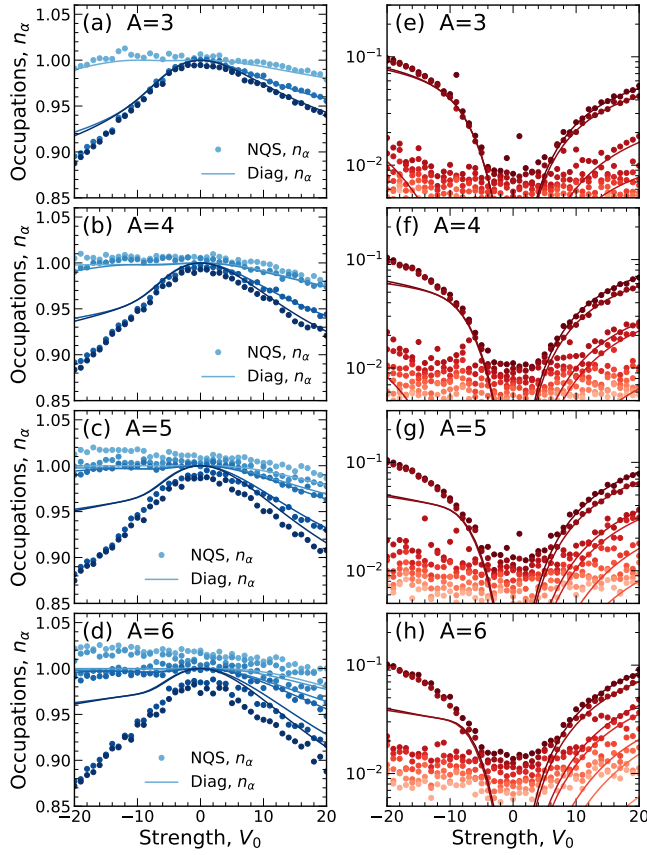


FIG. 12. Panels (a)-(d): hole ( $\alpha < A$ ) occupation probabilities for the  $A = 3$  (top row) to the  $A = 6$  (bottom row) systems as a function of interaction strength  $V_0$  for a fixed range  $\sigma_0 = 0.5$ . We compare NQS results (solid circles) to the direct diagonalisation predictions (solid lines). Panels (e)-(h): the same, in logarithmic scale, for particle ( $\alpha \geq A$ ) states up to  $\alpha = 14$ .

nature of the correlations in the repulsive and attractive sides of the spectrum. Clearly, the bosonic transition in the attractive side leads to a very strong rearrangement of the density profile. This rearrangement is so strong, in fact, that the direct diagonalisation based on non-interacting single-particle states struggles to capture it. An accurate description of this transition requires instead the solution of the system in real (or, possibly, momentum) space. In contrast, the rearrangement of the density in the repulsive regime mostly leads to a localisation of single-particle states that exaggerates the associated fermionic features. The HF approach in this limit, however, overestimates the fermionic features. The correlation energy in the repulsive side of the spectrum may be partially accounted for in terms of a renormalization of  $n(x)$ .

### 3. Occupation numbers

We get further insight on the correlation structure of the system by looking at the occupation numbers,  $n_\alpha$ , for different single-particle states  $\alpha$ . We show  $n_\alpha$  for systems with  $A = 3$  (top row) to  $A = 6$  (bottom row) in Fig. 12. The left (right) hand panels correspond to the occupation probabilities of holes (particles),  $n_{\alpha < A}$  ( $n_{\alpha \geq A}$ ). There are distinct common structures appearing in the occupation numbers in the attractive and the repulsive regimes. In the attractive case, the NQS predicts the appearance of one doubly-degenerate state that becomes substantially depleted as  $V_0$  becomes more and more negative. This result is commensurate with the direct diagonalisation occupation prediction, which also appears to be double degenerate, although, somewhat less depleted. We interpret the difference between the NQS and the direct diagonalization prediction, again, as a sign of the truncated model space. Both the NQS and the diagonalisation predictions indicate that the remaining  $A - 2$  hole states are fully occupied to within a 2% accuracy, although, the statistical noise floor in the NQS approach makes it difficult to quantify this statement.

The particle states shown in panels (e)-(h) show the appearance of a doubly-degenerate state in the repulsive regime for all values of  $A$ . According to the NQS prediction, these states reach an occupation of  $\approx 10\%$  at  $V_0 = -20$ . These doubly-degenerate states are reminiscent of a bosonization of the fermionic degrees of freedom. This happens in spite of the absence of active spin degrees of freedom and hence can only be observed in the case of a finite-range interaction. Doubly-degenerate structures in the attractive regime have also been observed in variational calculation of one-dimensional  $p$ -wave fermions [38]. These simulations, however, have a harder time describing the repulsive regime, which the NQS can access seamlessly.

In the repulsive regime,  $V_0 > 0$ , no double degeneracy is observed. Single-hole states [panels (a)-(d)] and single-particle states [panels (e)-(h)] are all distinct, and one can clearly distinguish  $A$  states on the repulsive branch of each panel. This prediction is supported both by the direct diagonalisation and the NQS results. For the  $A = 3$  system, panel (a), we find that 3 distinct single-hole states appear with small depletions, with occupations of more than 95% up to  $V_0 \approx 20$ . The corresponding single-particle states in panel (e) are clustered into two nearly-degenerate states with populations of  $\approx 5\%$  at  $V_0 \approx 20$ , and another state with a population of 2%. A similar picture emerges as  $A$  increases. For even values of  $A$ , we find that there is a near (but not complete) degeneracy of  $A/2$  states. In the single-hole cases, the occupations decrease steadily with  $V_0$  in pairs. Similarly, the occupation of particle states increases in pairs of similar values. For odd  $A$ , the picture is essentially the same, except that there is an odd single-particle orbital with a specific occupation probability. We note that there are similarities between this picture and the results

obtained in Ref. [52] for a 1D spin-polarized trapped fermions with harmonic pair interactions.

For both the single-particle and single-hole states, the statistical noise floor is on the order of  $\approx 10^{-2}$ . We find a slight increase of this floor with particle number, of about a factor of 2 when moving from  $A = 3$  to  $A = 6$ . Although one can see the statistical noise within the single-particle states, their effect is even more evident in the single-hole states, where they lead to non-physical fluctuations with  $n_\alpha > 1$ . We arbitrarily limit the number of single-particle states to 14 within this analysis. The noise floor is consistent for all values of  $V_0$ , indicating that the source of the noise floor stems from the stochastic methodology used to calculate the OBDM. We limit the range of occupation values shown for the single-hole states to be above  $5 \times 10^{-3}$ , which highlights a few of the lowest single-hole states obtained with the direct diagonalisation approach (solid lines).

#### 4. One-body density matrix

So far, we have discussed local properties of the system. We now turn our attention to non-local structures reflected in the density matrices. In Fig. 13, we show the OBDM  $\rho(x'_1, x_1)$  of the ground-state wavefunction for  $A = 2$  (top row) to  $A = 6$  (bottom row). The different columns correspond to interaction strengths values from  $V_0 = -20$  to 20 (in steps of 10). The central panels correspond to the non-interacting case,  $V_0$ , which can be understood in relatively simple analytical tools from a combination of Eq. (26), valid in the non-interacting case, and the HO eigenstates of Eq. (3). In all cases, the density matrix is purely real, and covers a more or less square area in the  $x'_1 - x_1$  plane. This is a consequence of the combination of single-particle terms  $\varphi_n^*(x'_1)\varphi_n(x_1)$  in the sum of Eq. (26), which naturally provide a limit both within and outside the diagonal of the  $x'_1 - x_1$  plane [83]. Moreover, one finds that there is a relatively narrow area of positive values near the diagonal, where  $\rho(x' = x, x) \equiv n(x) > 0$ , is positive definite. As one moves away from the diagonal, definite ripples appear in areas with consecutive positive and negative values. These ripples reflect the nodal structure of the single-particle states. In fact, there are as many changes of sign along the  $x'_1 = -x_1$  direction as particles in the system.

In the attractive case, shown in the left panels, the overall size extent of the system decreases (see Fig. 10). Similarly, the support of the OBDM in the  $x'_1 - x_1$  plane also diminishes. Moreover, the peaks and troughs associated to the changes of sign in the off-diagonal direction move closer to the diagonal. Importantly, these interference effects appear to increase in magnitude as the interaction strength becomes more negative. We stress that the diagonalisation of this strongly oscillating OBDM leads to occupation numbers with a dominant doubly-degenerate structure, more reminiscent of a coherent picture.

In the strongly repulsive case, in the panels on the

right, one can clearly distinguish the localization of single-particle orbitals along the diagonal in the form of well-defined equidistant peaks. The off-diagonal oscillations and change of signs observed in the non-interacting and the attractive regimes, are substantially damped in this case. At  $V_0 = 20$ , for instance, one only observes a well defined series of  $A - 1$  patches with negative values. While there are additional oscillations along the off-diagonal direction, these have a much smaller amplitude, to the point that they can hardly be distinguished in the scale of the figure.

#### 5. Pair correlation function

Finally, we present in Fig. 14, the pair correlation function,  $g(x_1, x_2)$  of Eq. (11) for different particle numbers. The panels are organised in the same way as Fig. 13. The pair correlation function provides information of correlations due both to the antisymmetric nature of the system and to the presence of interactions [50]. The function  $g(x_1, x_2)$  is very different in the attractive and the repulsive regimes, but there are common structures across all panels. Specifically, we find a ridge around  $x_1 \approx x_2$  where the pair correlation vanishes. This is a consequence of the Pauli exclusion principle, which in the spinless fermion case imposes the condition  $g(x, x) = 0$ . In the non-interacting case, the condition is enforced by the  $(x_1 - x_2)^2$  term of Eq. (12). The width of this “Pauli” ridge, however, changes substantially with interaction strength, which indicates that part of it is also a consequence of interaction effects. On the panels to the right of the center, one clearly finds that the ridge becomes wider with  $V_0$ . This effect is a reflection of the spatial localisation of the orbitals observed in Figs. 6 and 10. We expect the size of the ridge in the repulsive side to be sensitive to both  $V_0$  and the range of the interaction,  $\sigma_0$ .

In contrast, on the attractive regime displayed on the left panels of the figure, we find that the ridge becomes narrower as  $V_0$  becomes more attractive, to the point that, for  $A > 5$ , the ridge is difficult to see on the leftmost panels with  $V_0 = -20$ . The pair distribution function in the attractive side is relatively featureless and, other than the ridge, it is extremely peaked in an almost square region around the center. This indicates a high likelihood of finding one particle in a region within a few units of position of the center, a picture that is reminiscent of a Bose-Einstein condensate. This picture is in line with the correlation structure of  $p$ -wave fermions observed in Ref. [38].

In contrast to this relatively featureless peak,  $g(x_1, x_2)$  on the repulsive side has a much richer structure, with several well-defined peaks. These peaks are clear indications of the emerging crystalline structure of the system, and have been observed in analogous simulations of one-dimensional, few-body Wigner crystals [73]. For odd particle numbers, we find that there is always a peak to the right (or left) of the Pauli ridge along the  $x_1 = 0$

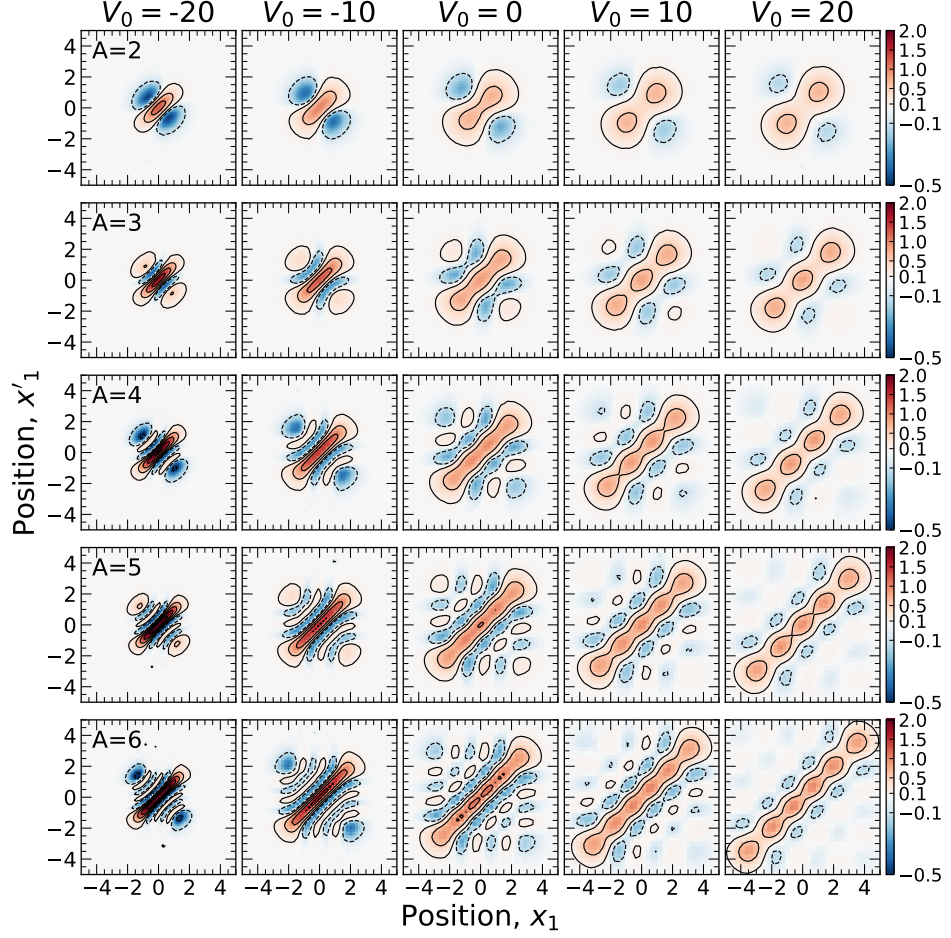


FIG. 13. Density contour plots of the one-body density matrix  $\rho(x'_1, x_1)$  of systems from  $A = 2$  (top row) to  $A = 6$  (bottom row) particles. Columns correspond to different interaction strengths, from  $V_0 = -20$  (left column), to  $V_0 = 20$  (right). Contours are shown at density matrix values of  $-0.5, -0.1, 0.1, 0.5, 1.0, 1.5$  and  $2.0$ . The colour coding is the same across all panels.

direction. For these systems, the density has a peak at  $x = 0$ , so one particle sitting at  $x_1 = 0$  will have a large probability of finding  $A - 1$  particles at fixed intervals in  $x_2$ . For  $A = 3$ , this occurs at  $x_2 = \pm 2$ , whereas for  $A = 5$  this happens at about  $x_2 = \pm 2$  and  $\pm 4$ . For an even number of particles, there is a depletion in the density distribution at the center of the trap, see Figs. 6 and 10. Consequently, the pair correlation function along  $x_i = 0$  does not show any peaks. Instead, the lines of  $A - 1$  peaks are found at around  $x_i \approx \pm 1$ .

All in all, the pair correlation function for both systems indicates a well-defined crystalline phase in the repulsive regime, and a Bose-like phase in the attractive regime. This complex behaviour is obtained with an NQS formed by a single determinant with backflow correlations. In other words, for a fixed particle number, the same NQS is capable of describing systems with very different spatial extents, correlation structures and underlying physical pictures.

## V. CONCLUSION AND OUTLOOK

To conclude, we have applied the NQS method to solve the Schrödinger equation for one-dimensional systems of  $A$  harmonically-trapped, interacting fermions without spin degrees of freedom. We model the interaction using a gaussian form factor, motivated by potential nuclear physics applications, and such that in the zero-range limit we recover the non-interacting case. We purposely choose a set of interaction strengths and ranges where perturbation theory may not converge easily. In particular, we find that an interesting choice for the interaction range is half the natural oscillator length.

The NQS that we employ provides a fully antisymmetric ansatz to represent one-dimensional ‘spinless’ fermions. The NQS has two equivariant layers of  $H = 64$  hidden nodes each. These layers embed the one-dimensional positions of  $A$  particles into a  $H$ -dimensional space. These layers are then projected into a single GSD. This approach benefits from backflow correlations from the outset, and does not explicitly require a Jastrow factor. The number

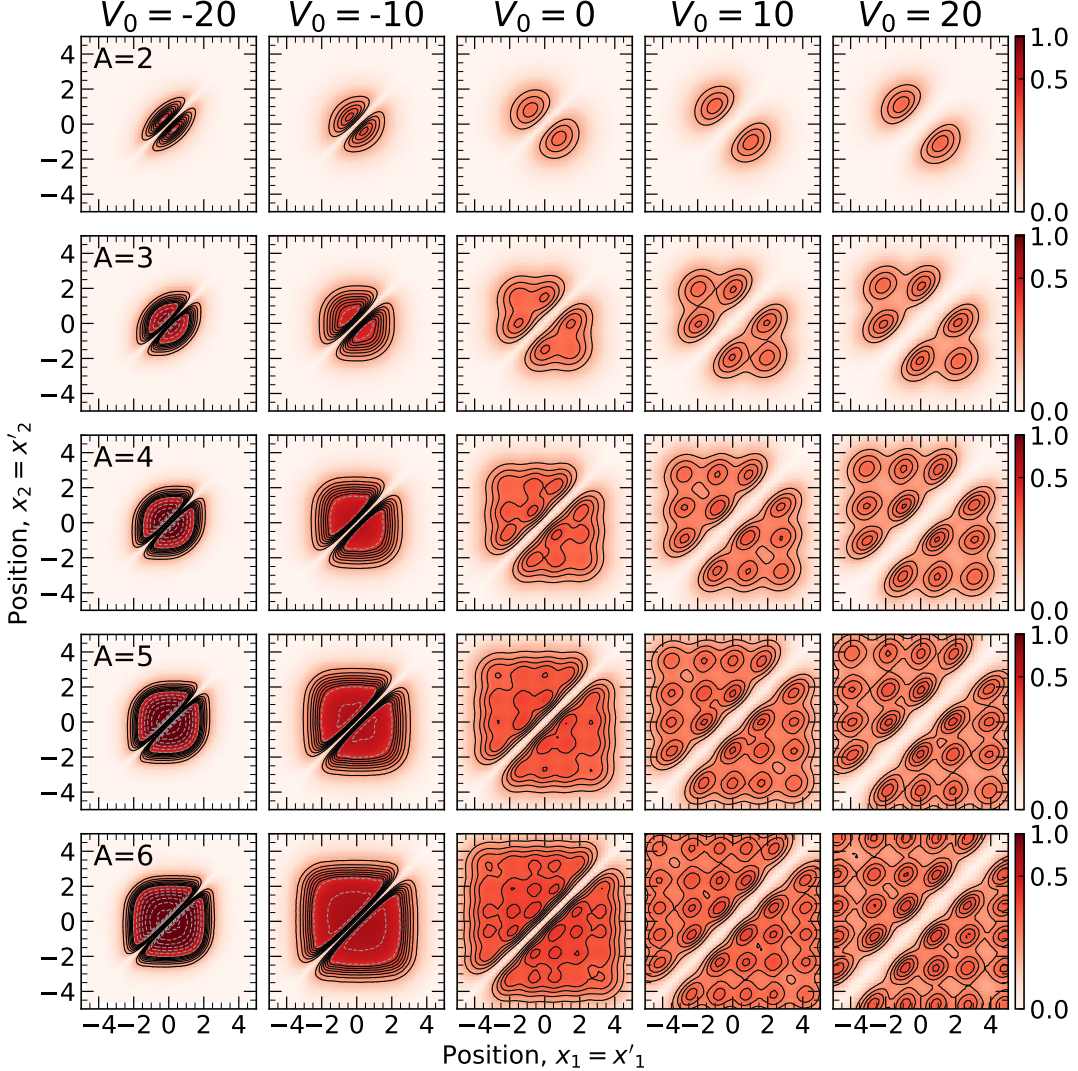


FIG. 14. Density contour plots of the pair correlation function  $g(x_1, x_2)$  for systems from  $A = 2$  (top row) to  $A = 6$  (bottom row) particles. Columns correspond to different interaction strengths, from  $V_0 = -20$  (left column), to  $V_0 = 20$  (right). Contours are shown at steps of 0.05 from 0 to 0.35 (solid lines), and at steps of 0.2 from 0.4 to 2 (dashed lines). The colour coding is the same across all panels.

of parameters of the NQS remains nearly constant when going from  $A = 2$  to  $A = 6$  particles. By combining the NQS with VMC techniques, we obtain a wavefunction that is able to represent many-body correlations and can accurately describe very different physical regimes without any specific modifications to the network architecture.

The focus of our paper is on benchmarking the new NQS approach with other well-known many-body methods. For all values of  $A$ , we compare against the mean-field Hartree-Fock method and the direct diagonalisation approach. Moreover, in the  $A = 2$  case we have access to an exact solution in real space as well as a perturbative treatment of the gaussian interaction. The results for all values of  $A$  indicate that the NQS can efficiently provide an accurate representation of the many-body wavefunction. One benefit of the NQS approach is its variational performance,

that surpasses mean-field approaches and does not suffer from basis truncation effects, like the direct diagonalisation method does. We characterise our benchmarking process using several properties, including the ground-state energy, density profiles, single-particle occupation numbers as well as the one-body density matrix and the pair correlation function.

The NQS can accurately describe the ground-state wavefunction across different physical regimes. In particular, we find two very different pictures that arise as the strength of the interaction goes from very attractive to very repulsive values. We find a common, method-independent interpretation for these two phases of 1D trapped spinless fermionic systems. On the attractive side, the density distribution of the system is a single peak centered at the origin, reminiscent of a Bose-Einstein

condensate. The peak becomes narrower and higher as the strength becomes more negative. This represents a substantial density rearrangement in the system, that is hard to capture with a truncated basis direct diagonalisation approach based on an harmonic oscillator basis. A real-space implementation of the Hartree-Fock, however, describes well this phase for sufficiently large  $A$ . In this regime, the one-body density matrix is strongly oscillating off the diagonal and the pair distribution function is narrow and squared-shape. We find that a degenerate set of 2 single-particle orbitals are strongly depleted, whereas the remaining  $A - 2$  states remain fully occupied.

In contrast, for large and repulsive values of the interaction strength we find a completely different picture. In this limit, we reach the regime of a crystal, and fermions spontaneously order in a periodic fashion. This is reflected in the density distribution, which has a well-defined periodic peak structure, with  $A$  peaks, as well as the pair correlation function, which shows associated crystalline structure peaks. In terms of occupation numbers, the repulsive regime exhibits quasi-degeneracies in pairs of orbitals. We note that this regime is well described by the direct diagonalisation approach, but the HF approximation predicts density distributions with exaggerated localisation features.

We foresee several applications of this work in the near future, and distinguish between applied and formal developments. On the applied side, we have found clear signatures of two physical phases in relatively simple fermionic systems. When spin is not present, finite-range interaction effects are necessary and lead to very different behaviours in the attractive and repulsive regime. Here, one may exploit NQSSs to investigate physical features that have not been explored here, like higher-order density matrices. Having access to the full wave function of the system, we should also be able to characterise the evolution of entanglement measures as a function of interaction parameters. It would be interesting to try and access these regimes experimentally. This is likely to occur near small values of the interaction range  $\sigma$  (e.g. the zero-range limit). We stress that there is no fundamental

limitation hampering the applicability of the NQS method in that limit.

On the formal side, there are interesting steps forward to take in a variety of directions. In applications of one-dimensional ultracold atoms, spin degrees of freedom are relevant, and often manipulated experimentally. This calls for an explicit, general spin-dependent representation of NQSSs, along the lines recently explored in lattice systems [84] and nucleons [29], but potentially applicable to  $SU(N)$  interactions. A comparison with the rich variety of experiments in non-perturbative regimes here may provide a fertile ground for tests of the applicability of NQS ansätze.

Our final aim is the study of nuclear physics systems employing NQSSs. To this end, we need to extend our current technology to treat three-dimensional systems. This also requires treatment of spin and isospin degrees of freedom. All studies so far indicate that nuclei in the few-body sector can be theoretically accessed by employing NQSSs [25, 27–29]. It remains to be seen whether the promising scaling with particle number that we have found in this work can be efficiently transferred into a nuclear physics setting and deliver a substantial change in *ab initio* nuclear theory.

## ACKNOWLEDGMENTS

This work is supported by STFC, through Grants Nos ST/L005743/1 and ST/P005314/1; by grant PID2020-118758GB-I00 funded by MCIN/AEI/10.13039/501100011033; by the “Ramón y Cajal” grant RYC2018-026072 funded by MCIN/AEI /10.13039/501100011033 and FSE “El FSE invierte en tu futuro”; and by the “Unit of Excellence María de Maeztu 2020-2023” award to the Institute of Cosmos Sciences, Grant CEX2019-000918-M funded by MCIN/AEI/10.13039/501100011033. TRIUMF receives federal funding via a contribution agreement with the National Research Council of Canada.

---

[1] G. Carleo, I. Cirac, K. Cranmer, L. Daudet, M. Schuld, N. Tishby, L. Vogt-Maranto, and L. Zdeborová, *Rev. Mod. Phys.* **91**, 045002 (2019), [arXiv:1903.10563](#).

[2] G. Cybenko, Mathematics of control, signals and systems **2**, 303 (1989).

[3] K. Hornik, *Neural Networks* **4**, 251 (1991).

[4] B. Irie and S. Miyake, in *ICNN* (1988) pp. 641–648.

[5] A. N. Kolmogorov, in *Doklady Akademii Nauk*, Vol. 114 (Russian Academy of Sciences, 1957) pp. 953–956.

[6] G. Carleo and M. Troyer, *Science* **355** (2017), 10.1126/science.aag2302, [arXiv:1606.02318](#).

[7] H. Saito, *J. Phys. Soc. Japan* **86**, 093001 (2017), [arXiv:1707.09723](#).

[8] H. Saito, *J. Phys. Soc. Japan* **87**, 074002 (2018), [arXiv:1804.06521](#).

[9] K. Choo, G. Carleo, N. Regnault, and T. Neupert, *Phys. Rev. Lett.* **121**, 167204 (2018), [arXiv:1807.03325](#).

[10] M. Rigo, B. Hall, M. Hjorth-Jensen, A. Lovato, and F. Pederiva, *Phys. Rev. E* **107**, 025310 (2023), [arXiv:2211.04614](#).

[11] B. Fore, J. M. Kim, G. Carleo, M. Hjorth-Jensen, and A. Lovato, arXiv preprint [arXiv:2212.04436](#) (2022).

[12] D. Pfau, J. S. Spencer, A. G. D. G. Matthews, and W. M. C. Foulkes, *Phys. Rev. Res.* **2**, 033429 (2020), [arXiv:1909.02487](#).

[13] J. S. Spencer, D. Pfau, A. Botev, and W. M. C. Foulkes, arXiv preprint [arXiv:2011.07125](#) (2020).

[14] J. Hermann, Z. Schätzle, and F. Noé, *Nat. Chem.* **12**, 891 (2020), arXiv:1909.08423.

[15] Z. Schätzle, J. Hermann, and F. Noé, *J. Chem. Phys.* **154**, 124108 (2021), arXiv:2010.05316.

[16] M. Wilson, N. Gao, F. Wudarski, E. Rieffel, and N. M. Tubman, arXiv preprint arXiv:2103.12570 (2021).

[17] M. Wilson, S. Moroni, M. Holzmann, N. Gao, F. Wudarski, T. Vegge, and A. Bhowmik, arXiv preprint arXiv:2202.04622 (2022).

[18] I. von Glehn, J. S. Spencer, and D. Pfau, arXiv preprint arXiv:2211.13672 (2022).

[19] M. Scherbelá, R. Reisenhofer, L. Gerard, P. Marquetand, and P. Grohs, *Nature Comp. Sci.* **2**, 331 (2022), arXiv:2105.08351.

[20] J. Hermann, J. Spencer, K. Choo, A. Mezzacapo, W. Foulkes, D. Pfau, G. Carleo, and F. Noé, arXiv preprint arXiv:2208.12590 (2022).

[21] K. Choo, A. Mezzacapo, and G. Carleo, *Nat. Commun.* **11**, 2368 (2020), arXiv:1909.12852.

[22] F. Vicentini, D. Hofmann, A. Szabó, D. Wu, C. Roth, C. Giuliani, G. Pescia, J. Nys, V. Vargas-Calderón, N. Astrakhantsev, and G. Carleo, *SciPost Phys. Codebases* **7** (2022).

[23] D. Ceperley, G. V. Chester, and M. H. Kalos, *Phys. Rev. B* **16**, 3081 (1977).

[24] A. Paszke, S. Gross, S. Chintala, G. Chanan, E. Yang, Z. DeVito, Z. Lin, A. Desmaison, L. Antiga, and A. Lerer, in *NIPS Autodiff Workshop* (2017).

[25] J. Keeble and A. Rios, *Phys. Lett. B* **809** (2020), 10.1016/j.physletb.2020.135743, arXiv:1911.13092.

[26] J. W. T. Keeble, *Neural Network Solutions to the Fermionic Schrödinger Equation*, Ph.D. thesis, University of Surrey (2022).

[27] C. Adams, G. Carleo, A. Lovato, and N. Rocco, *Phys. Rev. Lett.* **127**, 022502 (2021), arxiv:2007.14282.

[28] A. Gnech, C. Adams, N. Brawand, G. Carleo, A. Lovato, and N. Rocco, *Few-Body Systems* **63**, 7 (2022), arXiv:2108.06836.

[29] A. Lovato, C. Adams, G. Carleo, and N. Rocco, *Phys. Rev. Res.* **4** (2022), 10.1103/PhysRevResearch.4.043178, arXiv:2206.10021.

[30] M. Girardeau, *J. Math. Phys.* **1**, 516 (1960).

[31] M. Valiente, *Phys. Rev. A* **102**, 053304 (2020), arXiv:2009.00624.

[32] M. D. Girardeau, H. Nguyen, and M. Olshanii, *Opt. Commun.* **243**, 3 (2004), cond-mat/0403721.

[33] T. Sowiński and M. Ángel García-March, *Rep. Prog. Phys.* **82**, 104401 (2019), arxiv:1903.12189.

[34] A. Minguzzi and P. Vignolo, *AVS Quantum Science* **4**, 027102 (2022), arxiv:2201.02362.

[35] M. Girardeau and M. Olshanii, arXiv preprint cond-mat/0309396 (2003).

[36] M. D. Girardeau and M. Olshanii, *Phys. Rev. A* **70**, 023608 (2004).

[37] P. Kościuk and T. Sowiński, *Sci. Rep.* **8**, 48 (2018), arXiv:1707.04240.

[38] P. Kościuk and T. Sowiński, *New J. Phys.* **22**, 093053 (2020), arXiv:2004.06610.

[39] I. Bloch, J. Dalibard, and W. Zwerger, *Rev. Mod. Phys.* **80**, 885 (2008), arxiv:0704.3011.

[40] S. Giorgini, L. P. Pitaevskii, and S. Stringari, *Rev. Mod. Phys.* **80**, 1215 (2008), arxiv:0706.3360.

[41] B. DeMarco and D. S. Jin, *Science* **285**, 1703 (1999).

[42] N. Navon, S. Nascimbène, F. Chevy, and C. Salomon, *Science* **328**, 729 (2010), arxiv:1004.1465.

[43] A. N. Wenz, G. Zürn, S. Murmann, I. Brouzos, T. Lompe, and S. Jochim, *Science* **342**, 457 (2013), arxiv:1307.3443.

[44] A. Rojo-Francàs, A. Polls, and B. Juliá-Díaz, *Mathematics* **8**, 1196 (2020), arXiv:2005.10886.

[45] Y. Suzuki and K. Varga, *Stochastic Variational Approach to Quantum-Mechanical Few-Body Problems* (Springer-Verlag Berlin Heidelberg, 1998).

[46] P. Ring and P. Schuck, *The Nuclear Many-Body Problem* (Springer, Berlin, Heidelberg, 1980).

[47] A. Kievsky, M. Gattobigio, L. Girlanda, and M. Viviani, *Annu. Rev. Nucl. Part. Sci.* **71**, 465 (2021), arXiv:2102.13504.

[48] L. Mitas, *Phys. Rev. Lett.* **96**, 240402 (2006), arXiv:cond-mat/0601485.

[49] P.-O. Löwdin, *Phys. Rev.* **97**, 1474 (1955).

[50] M. J. Knight, H. M. Quiney, and A. M. Martin, *New J. Phys.* **24**, 053004 (2022), arXiv:2106.09187.

[51] C. Schilling, *Phys. Rev. A* **88**, 042105 (2013), arXiv:1307.6858.

[52] C. Schilling and R. Schilling, *Phys. Rev. A* **93**, 021601 (2016), arXiv:1508.04452.

[53] E. K. U. Gross, E. Runge, and O. Heinonen, *Many-Particle Theory* (IOP Publishing, Bristol, 1991).

[54] A. Sannai, Y. Takai, and M. Cordonnier, arXiv preprint arXiv:1903.01939 (2019).

[55] R. M. Martin, L. Reining, and D. M. Ceperley, “Many-body wavefunctions,” in *Interacting Electrons: Theory and Computational Approaches* (Cambridge University Press, 2016) p. 122–143.

[56] F. Becca and S. Sorella, *Quantum Monte Carlo Approaches for Correlated Systems* (Cambridge University Press, 2017).

[57] M. Hutter, arXiv preprint arXiv:2007.15298 (2020).

[58] N. Metropolis and S. Ulam, *J. Am. Stat. Assoc.* **44**, 335 (1949).

[59] W. K. Hastings, *Biometrika* **57**, 97 (1970).

[60] D. P. Kingma and J. Ba, arXiv preprint arXiv:1412.6980 (2014).

[61] S.-X. Zhang, Z.-Q. Wan, and H. Yao, arXiv preprint arXiv:1911.09117 (2019).

[62] A. Scemama, T. Lelièvre, G. Stoltz, E. Cancès, and M. Caffarel, *J. Chem. Phys.* **125**, 114105 (2006), arXiv:cond-mat/0606439.

[63] J. Keeble, “Spinless fermions,” <https://github.com/jwtkeebles/SpinlessFermions> (2023).

[64] P. Mujal, E. Sarlé, A. Polls, and B. Juliá-Díaz, *Phys. Rev. A* **96**, 043614 (2017), arXiv:1707.04166.

[65] M. Płodzień, D. Wiater, A. Chrostowski, and T. Sowiński, arXiv preprint arXiv:1803.08387 (2018).

[66] J. W. Negele and H. Orland, *Quantum Many-Particle Systems* (Addison-Wesley, 1987).

[67] C. C. Marston and G. G. Balint-Kurti, *J. Chem. Phys.* **91**, 3571 (1989).

[68] “One-dimensional spinless fermions,” [https://github.com/arnaurios/1D\\_fermions](https://github.com/arnaurios/1D_fermions) (2023), github repository.

[69] T. Busch, B. G. Englert, K. Rzazewski, and M. Wilkens, *Found. Phys.* **28**, 549 (1998).

[70] B. L. Earl, *J. Chem. Ed.* **85**, 453 (2008).

[71] J.-P. Blaizot and G. Ripka, *Quantum theory of finite systems* (MIT Press, Cambridge, Massachusetts, 1986).

[72] E. Wigner, *Phys. Rev.* **46**, 1002 (1934).

- [73] K. Jauregui, W. Häusler, and B. Kramer, *EPL* **24**, 581 (1993), arXiv:cond-mat/9305034.
- [74] B. Szafran, F. M. Peeters, S. Bednarek, T. Chwiej, and J. Adamowski, *Phys. Rev. B* **70**, 035401 (2004), cond-mat/0405350.
- [75] I. Shapir, A. Hamo, S. Pecker, C. P. Moca, Ö. Leg-eza, G. Zarand, and S. Ilani, *Science* **364**, 870 (2019), arXiv:1803.08523.
- [76] D. Vu and S. Das Sarma, *Phys. Rev. B* **101**, 125113 (2020), arXiv:1901.00019.
- [77] N. Ziani, F. Cavaliere, K. Becerra, and M. Sassetti, *Crystals* **11** (2020), 10.3390/cryst11010020.
- [78] N. D. Drummond, Z. Radnai, J. R. Trail, M. D. Towler, and R. J. Needs, *Phys. Rev. B* **69**, 085116 (2004), arXiv:0801.0377.
- [79] B. E. Granger and D. Blume, *Phys. Rev. Lett.* **92**, 133202 (2004), cond-mat/0307358.
- [80] M. Valiente, *Phys. Rev. A* **103**, L021302 (2021), arXiv:2009.00614.
- [81] I. Morera, B. Juliá-Díaz, and M. Valiente, arXiv preprint arXiv:2103.16499 (2021).
- [82] W. L. McMillan, *Phys. Rev.* **138**, A442 (1965).
- [83] A. Rios, B. Barker, M. Buchler, and P. Danielewicz, *Ann. Phys.* **326**, 1274 (2011), arXiv:1009.0215.
- [84] J. Robledo Moreno, G. Carleo, A. Georges, and J. Stokes, *Proc. Natl. Acad. Sci.* **119** (2022), 10.1073/pnas.2122059119, arxiv:2111.10420.